

Deep Generative Model for Human Mobility Behavior

Ye Hong^{a,*}, Yatao Zhang^{a,b}, Konrad Schindler^c, Martin Raubal^{a,b}

^a*Institute of Cartography and Geoinformation, ETH Zurich*

^b*Future Resilient Systems, Singapore-ETH Centre, ETH Zurich*

^c*Photogrammetry and Remote Sensing, ETH Zurich*

Abstract

Understanding and modeling human mobility is central to challenges in transport planning, sustainable urban design, and public health. Despite decades of effort, simulating individual mobility remains challenging because of its complex, context-dependent, and exploratory nature. Here, we present MobilityGen, a deep generative model that produces realistic mobility trajectories spanning days to weeks at large spatial scales. By linking behavioral attributes with environmental context, MobilityGen reproduces key patterns such as scaling laws for location visits, activity time allocation, and the coupled evolution of travel mode and destination choices. It reflects spatio-temporal variability and generates diverse, plausible, and novel mobility patterns consistent with the built environment. Beyond standard validation, MobilityGen yields insights not attainable with earlier models, including how access to urban space varies across travel modes and how co-presence dynamics shape social exposure and segregation. Our work establishes a new framework for mobility simulation, paving the way for fine-grained, data-driven studies of human behavior and its societal implications.

Human mobility is inherently complex and often appears unstructured. From day to day, individuals visit locations across various spatial scales, using multiple transport modes at different periods of the day to engage in a range of activities. Indeed, movement decisions involve intricate psychological planning [1] and are influenced by individual factors such as physical ability [2] and socioeconomic status [3]. Despite this complexity, human mobility is fundamentally constrained by physical infrastructures [4], such as road and rail networks, and heavily influenced by the surrounding environment [5, 6]. Ample empirical evidence demonstrates that mobility patterns follow simple scaling laws [7–10], and exhibit striking regularities, for instance regarding spatial location choices [11]. These collective regularities form the foundation for the realistic simulation of human mobility behaviors.

*Corresponding author

Email addresses: hongy@ethz.ch (Ye Hong), yatzhang@ethz.ch (Yatao Zhang), schindler@ethz.ch (Konrad Schindler), mraubal@ethz.ch (Martin Raubal)

Despite significant efforts and the importance of the task, simulating mobility behavior remains challenging. Current approaches to synthesizing disaggregated travel demand, such as the Equasim pipeline [12], the OASIS framework [13], and various other methods based on the principle of utility maximization [14, 15], focus on the desires for activity and temporal constraints of individuals, while largely overlooking the spatial patterns of those activities. Conversely, state-of-the-art mechanistic models, including the Container model [16], the exploration and preferential return (EPR) model [17], and more recent variants derived from them [18–20], faithfully reproduce scaling laws of location visits, yet their limited modeling capacity restricts them from capturing the interactions between individuals’ spatial preferences and their other movement decisions [21]. Neglecting those interactions can lead to misconceptions about individual space usage. This has far-reaching consequences for downstream applications that depend on accurate spatial modeling, such as sustainable transportation [22], human-centered urban design [23], and epidemic prevention [24].

Data-driven deep learning models offer a possible solution to these challenges. In recent years, learning-based models have revolutionized image and text processing [25]. Notably, natural language processing has experienced remarkable progress through new sequence processing techniques that excel at capturing complex patterns in large text collections, in particular, the transformer architecture [26] and the denoising diffusion probabilistic model (DDPM) [27, 28]. Their effectiveness in modeling language has facilitated applications across diverse domains concerned with spatial or temporal sequences, such as protein structures [29], turbulent flows [30], or human life events [31]. Individual mobility can be conceptualized as a sequence of discrete, time-ordered events, each reflecting concurrent behavioral decisions made during movement. Still, language models are not directly applicable to human mobility behavior. Generalizing deep generative modeling techniques, originally designed for one-dimensional word sequences, to the multifaceted nature of mobility behavior shaped by external contexts, requires careful consideration.

Here, we introduce MobilityGen, a deep generative model that simulates realistic, multifaceted human mobility over days and weeks and at large spatial scales. Recognizing that individual mobility unfolds as a sequence of events, MobilityGen leverages a DDPM to learn the generative mechanisms underlying these trajectories. Each event comprises multiple behavioral attributes, modeled as distinct but interdependent learning objectives, with their interactions captured through a shared latent representation that encodes meaningful structure across mode, time, and location. In addition, MobilityGen incorporates contextual features of the built environment. This allows the generation of realistic yet previously unseen behavioral variations. As our experiments show, the model reproduces national-scale visitation and transitions. It also captures behavioral dependencies that span extended temporal horizons, producing synthetic sequences

closely aligned with real-world patterns. Together, these capabilities establish a unified framework for mobility simulation, enabling the generation of comprehensive, fine-grained mobility data at scale and supporting analyses previously not feasible with earlier models. This facilitates applications ranging from testing sustainable transport strategies and assessing accessibility in urban design to analyzing co-presence dynamics that influence social segregation and epidemic response.

Results

A deep generative model of individual mobility

To identify individual mobility patterns and establish a comprehensive model, we analyzed GNSS trajectories from a smartphone-based travel survey that recorded the mobility behavior of thousands of participants across Switzerland. We focused on ≈ 2100 individuals who were continuously tracked over an extended period with high spatio-temporal accuracy (see Methods). For subsequent sequence modeling, GNSS traces are segmented into stationary periods, i.e., fixed locations where individuals perform activities, and movement sections corresponding to transits between these activity locations. We then calculate activity attributes (such as time use and travel mode) and project the activity locations onto a hierarchical multi-resolution grid, with the highest resolution being $\approx 500 \times 500 \text{m}^2$ per cell (exact size varies slightly due to cartographic projection, see Methods). Inspired by activity-based modeling methods [1], we conceptualize human mobility as sequences of activity events, each linked to specific attributes such as location, time use, and travel mode, along with contextual information (Figure 1a). We particularly focus on contexts that characterize the physical environment, including the coordinate geometry of locations and points of interest (POIs) that represent urban functional facilities.

The challenge for a comprehensive mobility model involves analyzing this multi-dimensional temporal data stream to derive realistic, multifaceted activity behavior. Traditional methods often focus on a single aspect, such as location choices [16] or travel mode preferences [32], or are limited to describing simple behavioral dependencies [12, 33]. In contrast, we propose MobilityGen, which jointly models these attributes and their relations with contextual information.

MobilityGen employs learnable embedding modules to map raw attributes and contexts to a shared embedding space (Figure 1b). Learning comprehensive mobility embeddings enables MobilityGen to decouple and thoroughly explore the intricate structure of activity events. We utilize a DDPM [27, 28] to transform latent embeddings into event sequences. This recent class of generative models has emerged as a particularly powerful scheme to learn complex, high-dimensional data distributions, thus capable of modeling

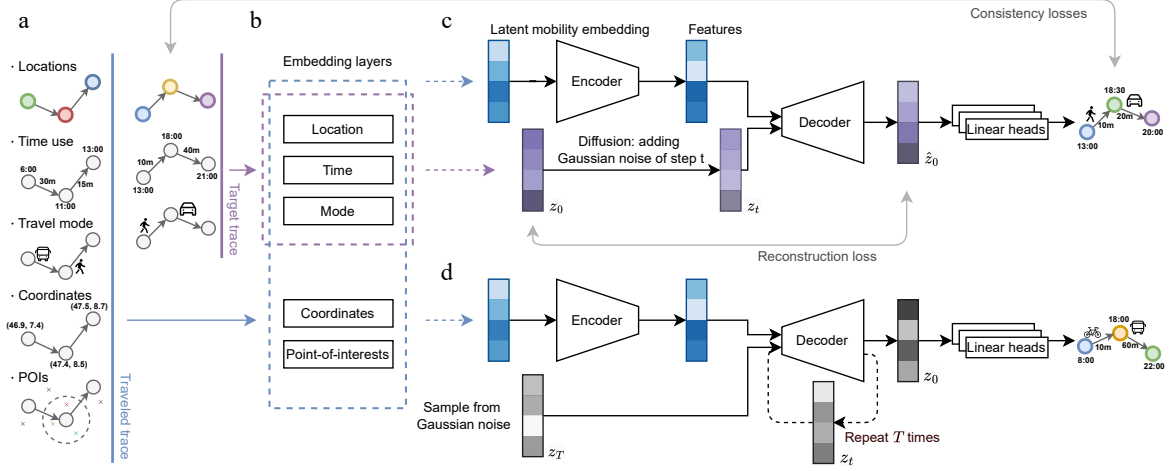


Figure 1: Modeling individual mobility with a deep generative framework. **a.** We conceptualize individual mobility as a sequence of chronologically ordered activity events, where each event has associated activity attributes (location, time use, and travel mode) and contextual information (coordinates and nearby POIs). **b.** Raw activity events are encoded into latent mobility embeddings through dedicated embedding modules. **c.** During training, the diffusion process adds Gaussian noise to the target sequence embedding \mathbf{z}_0 . A transformer-based decoder learns to reverse this process and reconstruct a denoised embedding $\hat{\mathbf{z}}_0$. Features from the traveled sequence are extracted by an encoder and provided as guidance to the decoder. Final activity attributes are predicted via linear output heads. The model is trained by minimizing reconstruction and consistency losses between the generated and original sequences (see Methods). **d.** During inference, we sample a Gaussian noise vector $\mathbf{z}_T \sim \mathcal{N}(0, \mathbf{I})$ and iteratively refine it using the decoder, guided by encoder-extracted features. The denoised embedding \mathbf{z}_0 is then decoded into the sequence of activity events. Travel mode icons adapted from Flaticon.com.

the mechanisms that govern these events. In a DDPM, the original sequence is gradually corrupted with tractable random noise, and an encoder-decoder network (in our case, a transformer [26]) learns the reverse denoising process (Figure 1c). Once trained, the (reverse) process can generate new, plausible sequences from pure Gaussian noise (Figure 1d). Additionally, MobilityGen uses a transformer encoder network to derive features from the observed traveled sequence, acting as a guiding signal during the denoising process for generating event embeddings. Finally, linear decoder heads extract the respective activity attributes from the predicted embeddings. Together, these attributes form the final output, namely a new, simulated sequence of activity events for an individual, sampled in a way that respects the observed transition and combination patterns of activity attributes.

Microscopic modeling reproduces location choice behavior

To demonstrate that the newly generated activity events replicate realistic mobility behaviors, we begin by evaluating the ability of MobilityGen to capture location patterns. How individuals select spatial locations for different activities shapes their interactions with physical space and is a fundamental driver of many urbanization-induced challenges [34–36]. Here, for every traveled sequence in the test dataset, we allow the trained MobilityGen to generate a synthetic sequence containing 50 activity events (see Methods). We

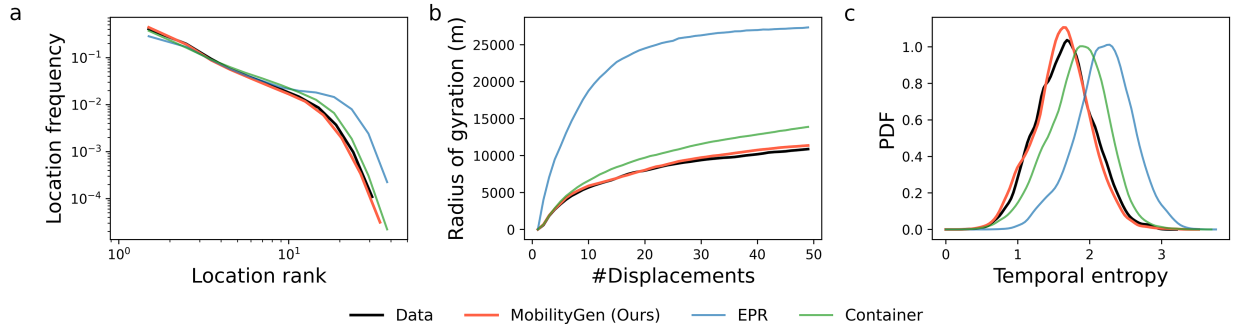


Figure 2: Evaluating microscopic mobility models with location metrics. **a.** Rank-frequency distribution of visited locations. **b.** Median radius of gyration as a function of the number of displacements. **c.** Distribution of temporal mobility entropy across individuals. All metrics are compared between real data (black), MobilityGen (red), EPR (blue), and Container (green). MobilityGen aligns most closely with empirical distributions across all metrics.

focus on the simulated visits to locations and compare them with the real visits from empirically observed sequences.

We first assess the ability of MobilityGen to capture fundamental properties of location choices and compare its performance against state-of-the-art microscopic mobility models. This is done through representative statistical location metrics, including the distribution of location visit frequency, the evolution of the radius of gyration, and the distribution of mobility entropy (see Methods). We evaluate each metric for real data and for location traces generated by MobilityGen, EPR [17], and Container [16] (Figure 2). We begin with the average rank distribution of location visits (Figure 2a), a widely used measure of preference for activity locations [8, 37]. Our results indicate that MobilityGen provides a significantly better fit to real data than both the EPR and Container models, as confirmed by the likelihood ratio test [38] (with $P < 10^{-3}$) and the Wasserstein distances [39] between the rank distributions (see Extended Data Table 1). The radius of gyration, which measures the characteristic distance an individual covers [8], serves to quantify the movement intensity in space. We observe that the median evolution of the radius of gyration across individuals, $r_u(k)$, over displacement steps k , is well described by logarithmic growth for both real and generated location sequences (Figure 2b), consistent with previous findings [16]. However, when fitting $r_u(k) \propto \alpha \log(k)$, only the value α derived from MobilityGen agrees well with the real data (see Supplementary Note 1). Finally, we evaluate the temporal mobility entropy that quantifies the predictability of location sequences, considering both the frequency and the order of visits [11]. Using the likelihood ratio test and the Wasserstein metric, we further confirm that, compared against the EPR and Container models, MobilityGen most accurately approximates the true entropy distribution over the population (with $P < 10^{-3}$, see Figure 2c and Extended Data Table 1). Additionally, we evaluated a representative set of state-of-the-

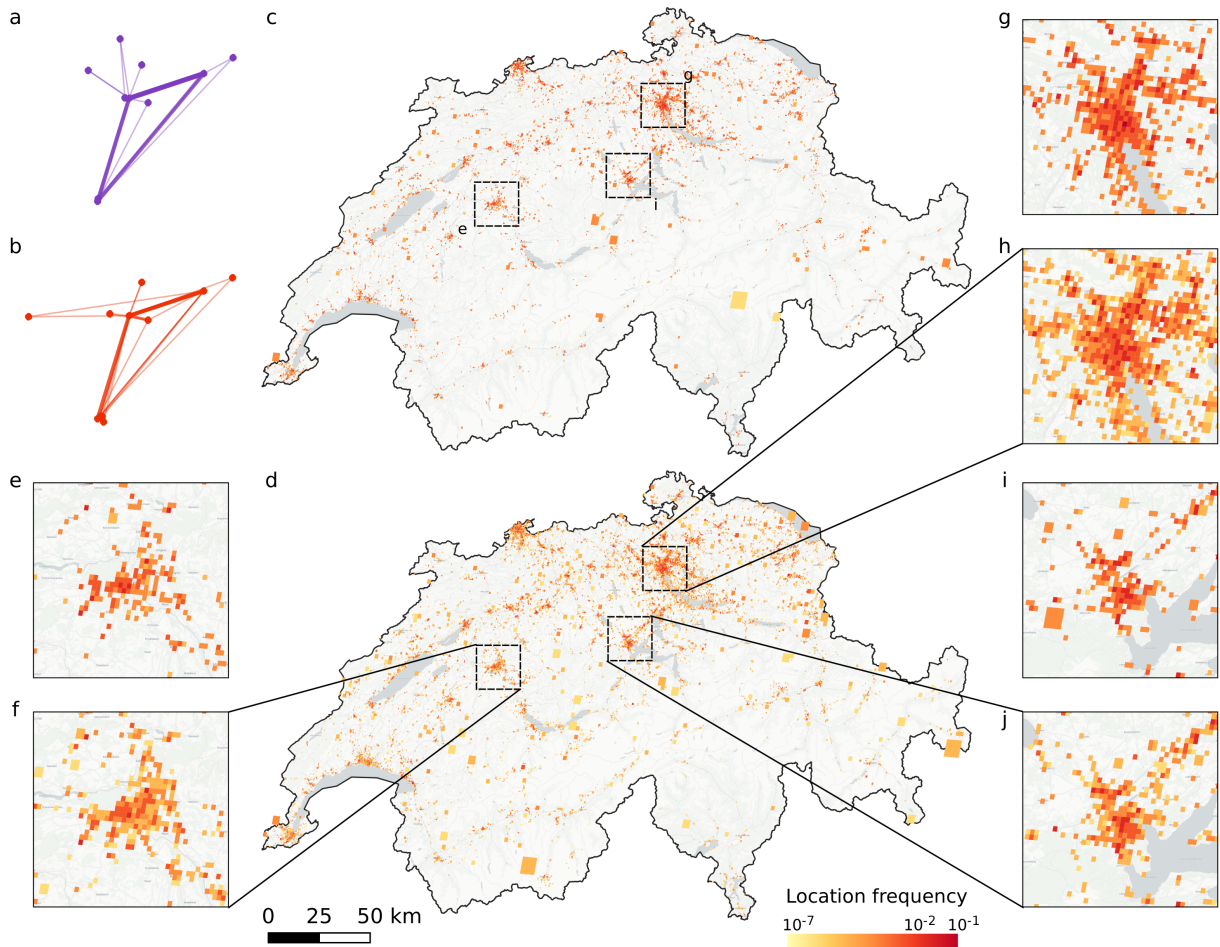


Figure 3: MobilityGen generates realistic spatial patterns of location visits across individual, urban, and national levels. We compare the spatial distribution of activity locations in real data (**a**, **c**, **e**, **g**, and **i**) with those generated by MobilityGen (**b**, **d**, **f**, **h**, and **j**). **a** and **b** show visits and transitions for a sample individual, where edge width is proportional to transition frequency. The generated sequence reflects routinely visited locations while also capturing exploratory behavior. **c** and **d** display aggregated visit frequencies across all individuals in Switzerland, with warmer colors indicating higher visitation intensity on a log scale. Panels **e**–**j** provide zoomed-in views for Bern (**e**, **f**), Zurich (**g**, **h**), and Lucerne (**i**, **j**). The generated sequences closely align with observed spatial patterns while exhibiting slightly greater diversity in the locations visited.

art data-driven mobility models and further location metrics (see Supplementary Note 1.1). Our findings indicate that MobilityGen consistently provides the best fit to real-world data. Further evaluations with metrics from language modeling confirm that MobilityGen can simulate location visits that closely resemble the real sequence while avoiding regurgitation of input sequences and maintaining sufficient diversity (see Supplementary Note 1.2).

To further evaluate the generated mobility patterns, we examine the spatial distribution of location visits. As an illustrative example, we map the observed and synthetic trajectories of a sample individual (Figure 3a and b). The comparison shows that MobilityGen effectively captures both visit and transition

patterns at frequently visited locations (thick lines), while also generating occasional visits to less familiar locations (thin lines). Accurately modeling such exploratory behavior remains a central challenge in human mobility research [40]. To assess how well MobilityGen addresses this challenge at the population level, we compare the aggregated spatial distribution of location visits across Switzerland in the real and simulated data (Figure 3c and d). Visit frequencies are color-coded from low (yellow) to high (red). MobilityGen closely matches the concentration of frequently visited locations and also generates visits to less frequented areas, reflecting a balance between individual-level exploration and population-level spatial preference. Using the entropy $E = -\sum_k p(f_k) \log p(f_k)$ to quantify the dispersion of location visits f_k , we obtain 0.33 for the real data and 0.53 for the simulated data, indicating greater spatial dispersion in the latter. To analyze spatial dynamics at a finer resolution, we examine three representative cities: Bern, Zurich, and Lucerne (Figure 3e-j), each characterized by distinct urban functions and mobility patterns. MobilityGen successfully reproduces key urban visitation structures in all three cases. However, spatial dispersion remains higher in the simulated data, with entropy values of 2.49 vs. 1.89 for Bern, 3.99 vs. 3.39 for Zurich, and 2.71 vs. 2.11 for Lucerne. Despite this discrepancy, MobilityGen compares favorably to other microscopic mobility models in replicating the location visit distributions (Extended Data Table 2). Complementary visual comparisons are provided at both national and urban levels in Extended Data Figure 1 and 2.

Structured behavioral patterns emerge across time, mode, and location

To move beyond location accuracy, we frame the mobility generation task as a multi-task learning problem that enables MobilityGen to jointly model a diverse set of behavioral attributes, including activity timing, travel mode, and interdependencies among attributes (see Methods). We evaluate the model’s ability to capture these structured patterns by generating 50 activity events for each sequence in the test set, focusing on behavioral regularities and attribute interactions (Figure 4).

Incorporating temporal information allows MobilityGen to reason about the scheduling of each activity. This temporal dimension is evident in the activity durations (Figure 4a) and the number of daily visited locations (Figure 4b), both of which closely match those observed in the real data. To further examine patterns of activity participation, we construct mobility motifs [41], which serve as high-level descriptors of regularities in activity location and scheduling. These motifs refer to unique topological structures that emerge when daily location visits are represented as graphs, with locations as nodes and trips between them as directed edges. From the real sequences, we identify eight motifs that occur on more than 0.5% of days (see Methods). MobilityGen accurately recovers the relative frequencies of both common and rare motifs, including simple two-location transitions and more complex patterns involving up to five locations

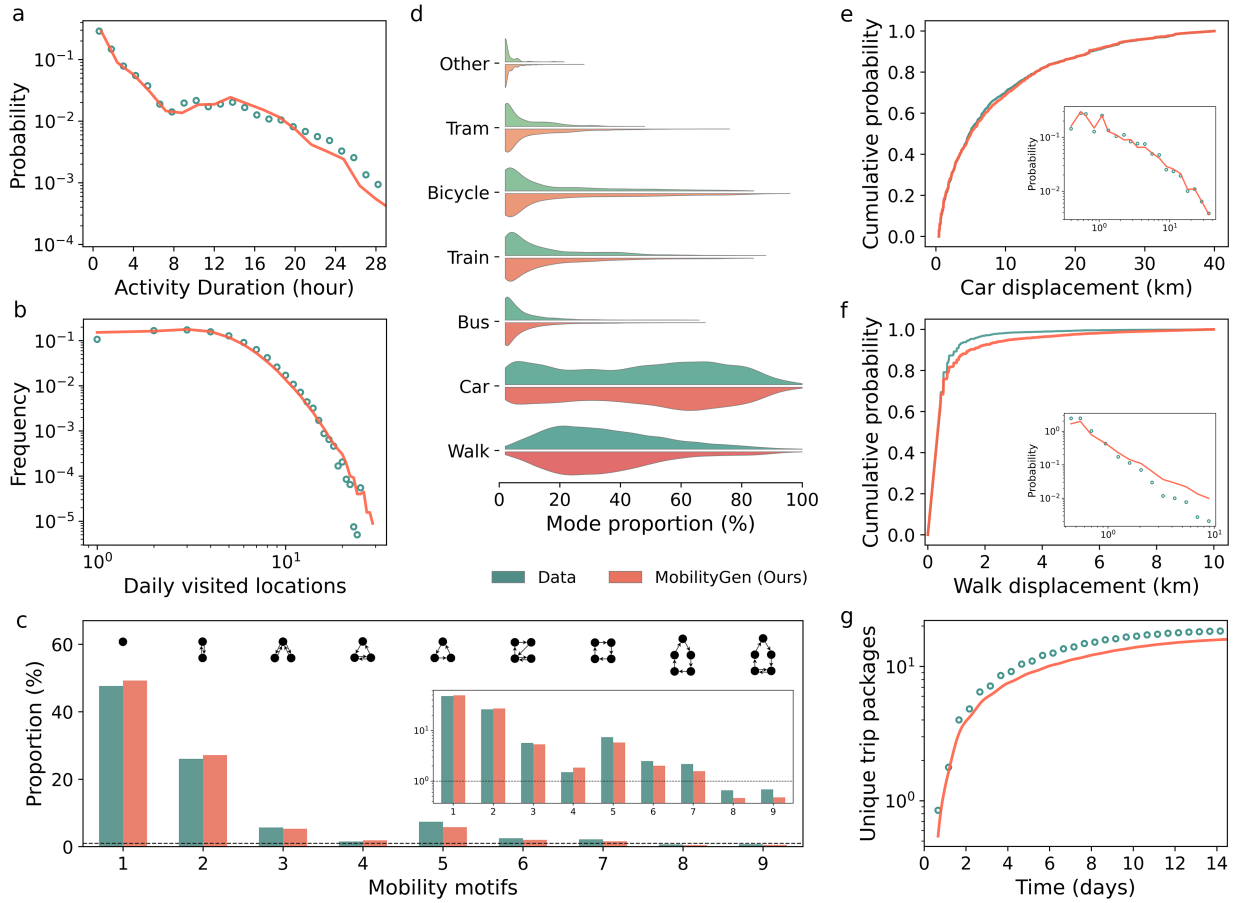


Figure 4: Generated activity events replicate individual activity-travel patterns across multiple dimensions. **a.** Distribution of activity durations. **b.** Distribution of daily visited locations. **c.** Distribution of mobility motifs, with motif diagrams shown above. The dashed line marks the 1% threshold as a visual guide, and the inset presents the same distribution on a log scale. **d.** Violin plots of modal shares across individuals. **e.** Cumulative distribution of car displacements, with the log-log distribution shown in the inset. **f.** Cumulative distribution of walk displacements, with the log-log distribution shown in the inset. **g.** Evolution of unique trip packages over time, averaged across individuals. Across all dimensions, the activity events generated by MobilityGen (red) closely align with empirical patterns from real-world data (green), capturing key behavioral regularities and attribute interactions.

(Figure 4c). We further benchmark MobilityGen against two state-of-the-art spatio-temporal mobility simulators, the Diary-based Trajectory Simulator (DITRAS) [42] and TimeGeo [33], using additional mobility metrics (see Extended Data Table 3 and Supplementary Note 2.1). Across all measures, MobilityGen more faithfully reproduces the interplay between activity timing and location choice, yielding the closest alignment with empirical behavior.

Next, we incorporate user-verified travel mode labels into MobilityGen to jointly model mode choice in relation to activity events. Figure 4d compares the travel mode distributions from the observed and simulated activity sequences, with discrepancies quantified by the Wasserstein distance (see Extended Data Table 3).

Across all scenarios, MobilityGen successfully reconstructs the mode preferences exhibited in real-world behavior. Car and walking, the two most common modes, show excellent agreement between empirical and simulated shares. Notably, MobilityGen also captures subtler distinctions among public modes, including bus, train, and tram, accurately reflecting their relative frequencies. We further assess mode-specific behavior by comparing the displacement distributions for car and walking trips (Figure 4e, f). For car travel, the simulated displacements closely align with the observed distribution (Kolmogorov–Smirnov statistic $KS = 0.02$, with $P < 10^{-3}$). For walking, MobilityGen produces slightly longer displacements ($KS = 0.06$, $P < 10^{-3}$), potentially due to short trips being disproportionately affected by spatial discretization. This effect could be mitigated in future work by adopting a finer location grid, although such refinement may increase computational complexity.

Finally, we assess the evolution of trip packages, defined as combinations of travel modes and activity locations [43], to evaluate MobilityGen’s ability to model complex attribute interactions (Figure 4g; see Methods). The average number of unique trip packages over time, denoted as $Tp(t)$, follows a sub-linear growth over time t , consistent with previous findings [43]. The scaling exponent α in the relation $Tp(t) \propto t^\alpha$ is nearly identical between simulated ($\alpha = 0.85 \pm 0.01$) and empirical sequences ($\alpha = 0.85 \pm 0.01$), indicating that MobilityGen accurately captures the evolving diversity of travel mode and activity location choices over time. Further ablation studies confirm that the full multi-attribute model achieves a more realistic representation of attribute interactions than simplified variants with fewer modeled attributes (see Supplementary Note 3.1).

To understand how MobilityGen captures attribute interactions and generates realistic activity sequences, we analyze the structure of its learned embedding space. We apply densMAP [44] to project the 128-dimensional embeddings into two dimensions for visualization (see Supplementary Note 2.2). The projections reveal that MobilityGen learns semantically meaningful representations: similar travel modes appear near each other, temporal attributes vary smoothly along continuous trajectories, and frequently visited locations are well-separated from infrequent ones. When multiple attributes are jointly embedded, the space reveals distinct event clusters tied to specific locations, alongside a more diffuse region that likely reflects less location-dependent activities. These patterns suggest that complex mobility dynamics can be inferred directly from behavioral sequences, with the embedding space offering a compact and interpretable representation that supports diverse mobility analysis.

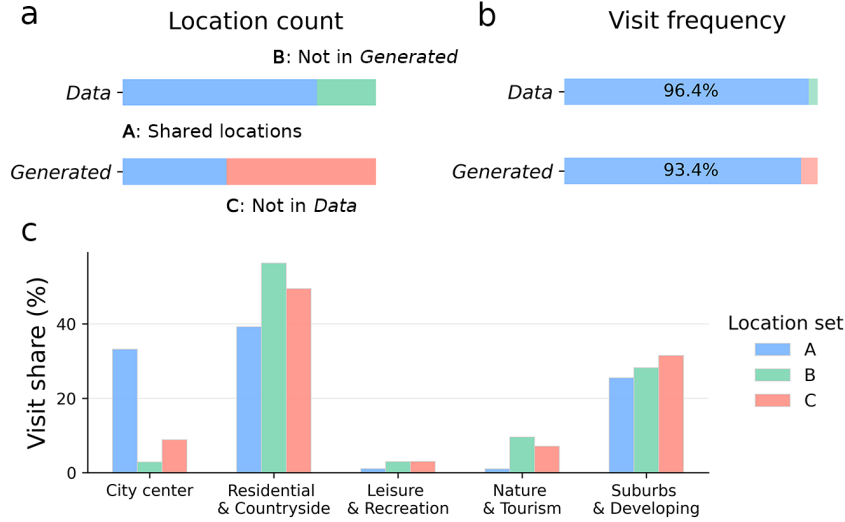


Figure 5: Point of Interest (POI) data supports the identification of locations associated with infrequent activities. **a.** We compare generated sequences with observed data, categorizing locations into those present in both (Set A), those found only in the data (Set B), and those found only in the generated sequences (Set C). **b.** As expected, locations in Set A are visited frequently, whereas those in Sets B and C are rarely visited. **c.** Relative visit frequencies by functional location type for each set. Functional types are inferred from POI distribution (see Methods). Sets B and C exhibit similar visit patterns, in contrast to the distribution observed for Set A.

Context enhances generalization to novel locations

A major feature of MobilityGen is its capacity to let contextual information influence individual travel decisions – an aspect well-supported by the literature but not adequately covered by existing microscopic mobility models [21]. In MobilityGen, these contexts are flexibly combined with activity attributes through learnable parameters, resulting in an implicit context-aware mobility model (Figure 1b, and see Methods). We restrict our analysis to spatial contexts that characterize the physical environment, namely the coordinate geometry, which reveals movement directionality [45]; and POIs, which display urban functions and imply movement purposes [46]. Further contexts could be integrated through appropriate representations; we defer this to future research.

We analyze location patterns to assess the influence of contextual factors on the simulation performance of MobilityGen. Generated locations are compared to observed data and categorized into three sets: Set A includes locations present in both sequences, while Sets B and C contain locations visited exclusively in the observed and generated sequences (Figure 5a). Since MobilityGen replicates key location preferences (see Figure 3), Set A is expected to capture the locations where individuals conduct most of their activities. Indeed, an analysis of the visit frequencies reveals that 96.4% of the true visits and 93.4% of the generated visits occur at locations in Set A (Figure 5b). In contrast, locations in Sets B and C receive relatively few

visits, reflecting individuals’ tendencies toward novelty-seeking and the exploration of unfamiliar locations [9, 17, 47].

To understand how MobilityGen models novelty-seeking behavior, we identify the functional types of locations using POI data. Applying k -means clustering to POI representations of locations yields five distinct location classes, whose functional types are inferred from their spatial distributions and the enrichment of specific POI categories [48, 49] (see Methods). This functional classification enables a detailed analysis of location preferences, revealing that visits in Set A predominantly occur in the *City center*, whereas visits in Sets B and C are largely concentrated in *Residential & Countryside*. Moreover, preferences for *Leisure & Recreation* and *Nature & Tourism* sites are markedly higher in Sets B and C than in Set A. Using pairwise Wasserstein distances to quantify the similarity of visitation patterns across sets, we find that Sets B and C are closely aligned (Wasserstein distance: 0.11), while their distributions differ substantially from that of Set A (Set A vs. Set B: 0.57; Set A vs. Set C: 0.56). In other words, MobilityGen effectively captures patterns of exploratory behavior, despite the inherent difficulty of characterizing novel locations and predicting which specific places individuals are likely to explore.

A comparison with a model that excludes contextual information confirms that incorporating context improves the ability to characterize locations (see Supplementary Note 3.1). This improvement is particularly relevant in settings where historical mobility information is limited, such as when individuals seek novel locations for their activities. To benchmark how effectively MobilityGen leverages contextual cues, we conducted comparative experiments against established mobility flow generation models: Gravity [50], Deep Gravity [51], and random forest [52]. These baselines estimate flows between location pairs using features such as distance, population, and selected facility densities (e.g., shops and transport hubs). Flow-based models differ fundamentally from MobilityGen in both problem formulation and modeling capacity. For instance, they cannot capture temporal dynamics or disaggregated mobility. To ensure a fair comparison, we focused exclusively on locations that were not observed during training (see Supplementary Note 3.2). The results show that MobilityGen outperforms the flow generation baselines by a substantial margin across multiple flow metrics (see Extended Data Table 4). We attribute this improved performance in novel locations to the integration of spatial features, including coordinate geometry and detailed POI information, as well as the joint modeling of contextual and behavioral factors. While further research is needed to fully understand novelty-seeking mobility, our findings support the hypothesis that comprehensive context modeling is necessary to capture the variability in human behavior.

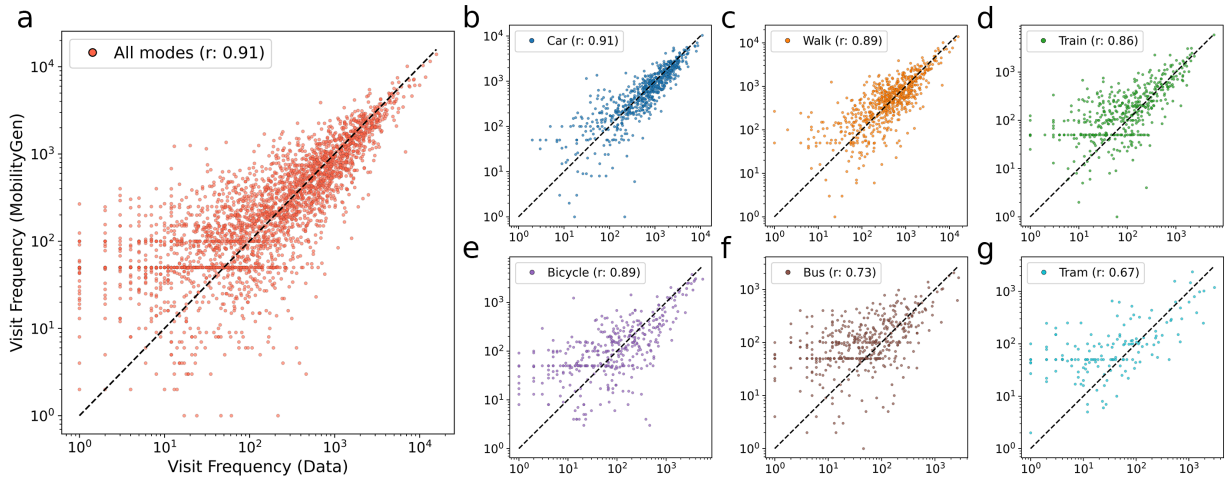


Figure 6: Reproducing location importance across travel modes. **a**. Visit frequencies for grouped locations in real and simulated activity events across all modes, showing strong overall agreement ($r = 0.91$, $P < 10^{-3}$). **b - g**. Mode-specific comparisons for car (**b**), walk (**c**), train (**d**), bicycle (**e**), bus (**f**), and tram (**g**). Each dot represents a group of locations with the same visitation frequency observed in the data. Diagonal lines denote perfect agreement. Higher agreement is observed for more frequently used modes (e.g., car and walk), while deviations increase for less common modes (e.g., tram).

Reproducing mode-specific spatial behavior and co-presence dynamics

Beyond standard validation, we ask whether the model enables analyses that have so far been difficult or infeasible with existing simulators. Our simulations generate realistic daily schedules that jointly capture where people go, how they travel, and when activities occur. Earlier tools often rely on predefined rules or cover only part of this behavioral structure, which has limited their use for studying differences across travel modes or patterns of shared presence in everyday settings. We focus on two representative scenarios with broad relevance to transport planning and urban research: (i) mode-specific spatial visitation, showing how individuals use different travel modes to move through urban space, and (ii) spatio-temporal co-presence, reflecting how individuals co-occur in space and time within shared environments.

Physical spaces serve distinct urban functions and inherently vary in importance. Some locations act as core anchors and attract frequent visits, while others are used more occasionally [10, 53]. MobilityGen faithfully captures this spatial heterogeneity. To demonstrate this, we compare simulated and real activity events by grouping locations according to their visitation frequency. The results show strong alignment (Pearson $r = 0.91$, $P < 10^{-3}$; Figure 6a), with important locations consistently retaining their prominence and highlighting the stability of core urban anchors. Crucially, MobilityGen enables analysis of how location importance differs across travel modes, a perspective not available in previous approaches. As shown in Figure 6b–g, agreement is highest for common modes such as car ($r = 0.91$) and walk ($r = 0.89$), while less frequent modes such as bus ($r = 0.73$) and tram ($r = 0.67$) show greater variation. These differences reveal

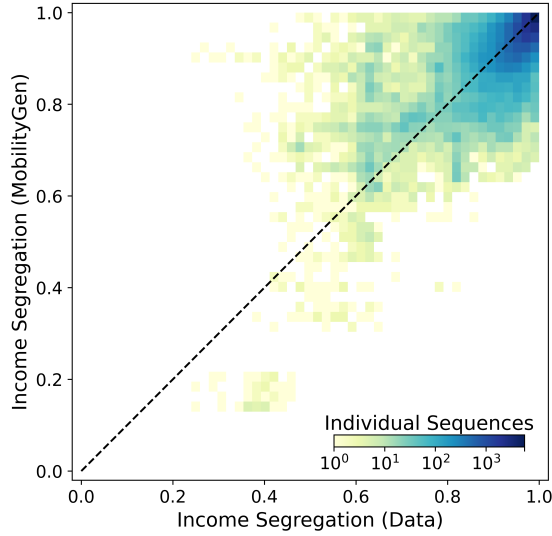


Figure 7: Reproducing individual-level income segregation from co-presence. Heatmap comparing segregation scores computed from observed and simulated activity events. Cell color indicates the number of individuals sharing each observed–simulated score pair. The diagonal line denotes perfect agreement. MobilityGen shows high agreement with empirical segregation patterns ($r = 0.70$, $P < 10^{-3}$).

how urban space is accessed unevenly across modes and underscore the challenge of simulating less frequent ones. Addressing this gap likely requires targeted modeling strategies and richer contextual data, particularly to better represent sustainable modes that are policy-relevant yet remain underutilized in practice. By capturing both stable urban anchors and variation in mode-specific access, MobilityGen enables new analyses of mode-aware demand, supporting applications from infrastructure usage modeling to accessibility assessments and scenario-based policy evaluation.

While spatial visitation captures where individuals go, co-presence patterns reveal whom they encounter, offering complementary insight into the intensity and distribution of interpersonal contact in daily urban life. A key application of co-presence lies in socio-spatial segregation research, where attention has shifted from static residential indicators to individual-level experienced segregation enabled by fine-grained mobility data [54]. We assess MobilityGen’s ability to reproduce these patterns by focusing on income-based segregation. Following Moro et al. [34], we group individuals into four income quantiles and measure, at each location, the time spent by people from different income groups (see Methods). We then calculate, for each individual, a segregation score that reflects their exposure to others across income levels. Simulated and observed segregation scores show strong agreement (Pearson $r = 0.70$, $P < 10^{-3}$; Figure 7), capturing both overall trends and the variability in co-presence-based income segregation. A breakdown by income quantiles confirms that MobilityGen reproduces systematic differences in exposure and substantially outperforms

baseline simulators such as TimeGeo and DITRAS, whose separation of space and time limits their ability to capture realistic contact patterns (see Extended Data Figure 4). This case study illustrates MobilityGen’s broader value as a generative model of social exposure. By capturing individual-level interactions in daily schedules, it provides a simulation environment to explore how population-level social mixing evolves under different scenarios. This extends beyond segregation analysis to domains such as information diffusion and infectious disease spread, where spatial co-presence fundamentally shapes outcomes.

Discussion

Despite growing interest in understanding human movement patterns and their implications, existing simulation models fail to capture the full spatio-temporal variability of mobility behavior. Here, we address this gap with MobilityGen, a deep generative model that produces realistic sequences of mobility events with detailed behavioral attributes. MobilityGen consistently outperforms baseline models across key mobility indicators and, crucially, generates novel behavioral interactions across time, space, and mode that earlier approaches cannot capture. It also enables analyses that were previously infeasible. By linking behavioral attributes with contextual information, MobilityGen uncovers how urban space is accessed differently across travel modes and how co-presence dynamics shape patterns of social exposure, such as income-based segregation. These examples show how generative modeling moves beyond reproducing standard metrics to open new avenues for research and policy enabled by fine-grained mobility data.

Our data-driven framework introduces a new paradigm for modeling individual mobility behavior. By integrating behavioral attributes into a shared latent space, MobilityGen captures their interactions across extended temporal and spatial scales. This facilitates the discovery of complex, longitudinal, and nuanced behavioral patterns that are otherwise difficult to model using traditional approaches. Looking ahead, MobilityGen could be combined with utility-based activity models in a hybrid approach, improving interpretability and allowing simulations that account for household activity participation and targeted mobility interventions. Its flexibility also supports the integration of richer contextual information, from detailed socio-demographic characteristics to social networks and environmental factors such as weather. Together, these extensions position MobilityGen as a bridge between mobility research and disciplines such as social, health, and environmental sciences, representing a step toward an integrative framework for interdisciplinary mobility modeling.

From a practical standpoint, MobilityGen generates long-term, realistic, and multifaceted activity schedules for individuals using GNSS tracking data, reducing the need for labor-intensive traditional travel surveys.

Generative mobility models offer several distinct advantages: they enable the creation of synthetic datasets at scales far beyond those of real-world collections and mitigate privacy concerns when analyzing or sharing disaggregated data. These large, openly accessible datasets, in turn, could promote the standardization and intercomparison of movement analysis methods. Finally, access to fine-grained synthetic mobility data could unlock previously unattainable simulation scenarios and studies in support of sustainable transport, urban planning, public health, and beyond.

Methods

Task formulation: activity event sequence generation

We focus on conditional mobility generation, aiming to simulate a sequence of future activity events $\mathbf{y} = [y_1, y_2, \dots, y_{k_1}]$ based on a preceding sequence of observed events $\mathbf{x} = [x_1, x_2, \dots, x_{k_2}]$ by the same individual. Each activity event x_i or y_i is represented as a tuple $\langle l, t, d, m \rangle$, where l denotes the location identifier, t the start time, d the duration, and m the travel mode. To incorporate spatial context, each event in the observed sequence \mathbf{x} is further associated with geographic coordinates g and land-use context c describing the surrounding environment.

Data sources and preprocessing

Mobility Data. MobilityGen was trained on a large-scale GNSS-based mobility dataset comprising high-resolution individual trajectories collected across Switzerland. The dataset contains billions of GNSS tracking records from approximately 3,700 individuals between 2019 and 2022, and was produced as part of the *Mobility Behaviour in Switzerland* (MOBIS) project, which investigates the behavioral impacts of mobility pricing [55]. Starting in autumn 2019, participants provided socio-demographic and travel-related information via a survey and recorded their movements over an eight-week period using a smartphone tracking app. The app collected GNSS samples triggered by motion events detected through onboard sensors (e.g., accelerometer). Following the main study, participants were invited to join the MOBIS-COVID extension, which assessed the impact of the COVID-19 pandemic on travel behavior. Roughly one-third of the original participants continued recording, with 730 individuals contributing data through the end of 2022. For further details on the study design and findings, see Molloy et al. [55].

We selected 2,113 individuals who had been tracked for at least 50 days and whose locations were known at least 60% of the time. This resulted in a dataset with an average tracking duration of 138 days and an average temporal coverage of 88% across individuals.

Extracting activity attributes. Human mobility diaries and activity attributes were derived from raw GNSS tracking records using the standard movement data model [56]. The tracking app analyzed motion metrics such as speed and acceleration from built-in smartphone sensors to segment GNSS traces into movement *stages* and stationary *staypoints*. Travel mode labels were inferred for each stage from the same motion data. During the tracking study, participants were encouraged to verify or correct the imputed mode labels and to annotate staypoints with their corresponding activity purposes. We identified *activity staypoints* as those where meaningful activities (e.g., home or restaurants) occurred, defined as stays longer than 25 minutes or carrying an activity label other than *waiting*. These staypoints were spatially aggregated into *locations*, representing repeated visits to the same place, using the Trackintel framework [57] with parameters $\epsilon = 20$ and $num_samples = 1$. The resulting locations were projected onto Google’s S2Geometry grid system, a hierarchical tessellation of the Earth’s surface. We used a progressive gridding strategy from level 10 (coarse) to level 14 (fine, with a spatial resolution of approximately $500 \times 500 \text{m}^2$), selecting a finer level when more than two locations were projected onto the same cell. This process yielded 142,575 location grids covering Switzerland, of which 28,742 were actively visited during the study period.

We define a *trip* as the sequence of consecutive movement stages between two activity staypoints and assign its primary travel mode as the one used for the longest stage (one of car, train, bus, tram, bicycle, walk, or other). In activity-based mobility analysis, travel is understood as a means to perform activities at different locations, making the activity itself the central unit of analysis [1]. Accordingly, we define each activity event with the following attributes: *start time* as the departure time of the preceding trip, *duration* as the sum of the trip and stay durations, and *travel mode* as the primary mode used to reach the activity location. The preprocessed dataset consists of 1,079,918 chronologically ordered activity events, each associated with a start time, duration, and travel mode, and spatially projected onto 28,741 unique locations.

External contextual data. We collected the point of interest (POI) dataset from OpenStreetMap (OSM) (<http://www.openstreetmap.org>), an open-source project that provides free and easily accessible digital map resources. Historical POI data for Switzerland were acquired from the end of 2022 to align with the time frame of the tracking dataset. The POI dataset was supplemented with OSM building data from the same year. For each building entry, we retained its attribute values but created a new POI by using the center point of its polygon geometry as its spatial representation. After removing redundant and insignificant POIs, the final dataset consisted of 3,104,590 POIs, categorized into 19 first-level and 188 second-level groups. The second-level categories, representing functional type descriptions, were used to obtain urban functions for

locations.

Data splits. We divided the activity event sequences into non-overlapping training, validation, and test sets in a 7:2:1 ratio based on time. Sequences occurring in the first 70% of tracking days for each individual were designated as training data, while the last 10% of days were used as test data. We considered mobility over the past three weeks as the traveled sequence and activity events in the subsequent week as the target sequence. The lengths of these sequences, as denoted by k_1 and k_2 , vary depending on the specific data. This process yielded 590,257, 104,010, and 36,285 pairs of traveled-target sequences for training, validation, and testing, respectively.

Diffusion-based modeling of discrete activity sequences

Diffusion models, grounded in non-equilibrium thermodynamics [27], are a class of likelihood-based deep generative models that excel at learning true data distributions and generating new data samples. These models have overcome several limitations of earlier approaches, with recent advancements in reparameterization [28] and inference efficiency [58] leading to breakthroughs in handling continuous data distributions, such as those in image and audio generation [59]. This progress has motivated researchers to extend the framework to discrete data, such as text, resulting in the development of discrete diffusion models for categorical distributions [60] and embedding diffusion models that incorporate additional discrete-to-continuous mapping steps [61, 62]. Here, we build on the conditional embedding DDPM by Li et al. [61] and generalize the framework to accommodate multifaceted mobility behavior.

The employed diffusion model introduces two Markov chains: a forward chain that progressively destructs data by injecting noise and a reverse chain that reconstructs the original data from noised samples. Formally, given a continuous data point \mathbf{z}_0 sampled from a real-world data distribution $q(\mathbf{z})$, i.e., $\mathbf{z}_0 \sim q(\mathbf{z})$, the forward Markov chain gradually corrupts \mathbf{z}_0 into a standard Gaussian noise $\mathbf{z}_T \sim \mathcal{N}(0, \mathbf{I})$ in $t \in [1, 2, \dots, T]$ steps:

$$q(\mathbf{z}_1, \dots, \mathbf{z}_T | \mathbf{z}_0) := \prod_{t=1}^T q(\mathbf{z}_t | \mathbf{z}_{t-1}) \quad (1)$$

where $\mathbf{z}_1, \dots, \mathbf{z}_T$ are the chain of noisy latent variables. For each forward step, the perturbation is controlled by adding Gaussian noise with a predefined step-dependent mean $\mu_t(\mathbf{z}_t) = \sqrt{1 - \beta_t} \mathbf{z}_{t-1}$, and variance $\Sigma_t(\mathbf{z}_t) = \beta_t \mathbf{I}$, with $\beta_t \in (0, 1)$:

$$q(\mathbf{z}_t | \mathbf{z}_{t-1}) := \mathcal{N}(\mathbf{z}_t; \sqrt{1 - \beta_t} \mathbf{z}_{t-1}, \beta_t \mathbf{I}) \quad (2)$$

Given the forward chain, the reverse denoising process aims to obtain $p_\theta(\mathbf{z}_{t-1} | \mathbf{z}_t)$, with which we can gradually reconstruct the original data \mathbf{z}_0 via sampling from \mathbf{z}_T and apply through a Markov chain:

$$p_\theta(\mathbf{z}_0, \dots, \mathbf{z}_T) := p(\mathbf{z}_T) \prod_{t=1}^T p_\theta(\mathbf{z}_{t-1} | \mathbf{z}_t) \quad (3)$$

where $p(\mathbf{z}_T) = \mathcal{N}(\mathbf{z}_T; 0, \mathbf{I})$. As the variance β_t is, by definition, small, the reverse process follows the same functional form as the forward process, i.e., a Gaussian distribution [27]:

$$p_\theta(\mathbf{z}_{t-1} | \mathbf{z}_t) := \mathcal{N}(\mathbf{z}_{t-1}; \mu_\theta(\mathbf{z}_t, t), \Sigma_\theta(\mathbf{z}_t, t)) \quad (4)$$

where the mean $\mu_\theta(\mathbf{z}_t, t)$ and variance $\Sigma_\theta(\mathbf{z}_t, t)$ are parameterized by deep neural networks with learnable parameters θ . Training is performed by maximizing the marginal likelihood of the data $\mathbb{E}[\log p_\theta(\mathbf{z}_0)]$, and the canonical objective is the variational lower bound \mathcal{L}_{vlb} of $\log p_\theta(\mathbf{z}_0)$ (for a detailed derivation of the objective, see Sohl-Dickstein et al. [27]):

$$\mathcal{L}_{vlb} = \mathbb{E}_{q(\mathbf{z}_1, \dots, \mathbf{z}_T | \mathbf{z}_0)} \left[D_{\text{KL}}(q(\mathbf{z}_T | \mathbf{z}_0) \| p(\mathbf{z}_T)) + \sum_{t>1} D_{\text{KL}}(q(\mathbf{z}_{t-1} | \mathbf{z}_t, \mathbf{z}_0) \| p_\theta(\mathbf{z}_{t-1} | \mathbf{z}_t)) - \log p_\theta(\mathbf{z}_0 | \mathbf{z}_1) \right] \quad (5)$$

where $D_{\text{KL}}(\cdot \| \cdot)$ denotes the Kullback–Leibler (KL) divergence, and $q(\mathbf{z}_{t-1} | \mathbf{z}_t, \mathbf{z}_0)$ is the forward process posterior, which follows a Gaussian distribution with mean $\hat{\mu}(\mathbf{z}_t, \mathbf{z}_0)$ and variance $\hat{\beta}\mathbf{I}$ that can be calculated from \mathbf{z}_0 , \mathbf{z}_t and β_t . The objective can be further simplified by reweighting each KL divergence term to obtain a mean-squared error reconstruction loss:

$$\mathcal{L}_{reconstruct} = \mathbb{E}_{\mathbf{z}_0, \mathbf{z}_t, t} \|\hat{\mathbf{z}}_\theta(\mathbf{z}_t, t) - \mathbf{z}_0\|^2 \quad (6)$$

Here, $\hat{\mathbf{z}}_\theta(\mathbf{z}_t, t)$ represents the prediction of the original data given \mathbf{z}_t and t . Intuitively, this parameterization can be interpreted as training a neural network to predict the original ground truth data from an arbitrarily corrupted version.

To apply continuous diffusion to discrete data, embedding diffusion models introduce an additional embedding process in the forward process and a rounding step in the reverse process. The embedding process transforms discrete tokens into a continuous latent space via a learnable embedding function, enabling the conventional diffusion process to be applied. Given the target sequence \mathbf{y} , the input \mathbf{z}_0 is obtained in the embedding space as $\mathbf{z}_0 \sim \mathcal{N}(\mathbf{e}_\phi(\mathbf{y}), \beta_0\mathbf{I})$, where $\mathbf{e}_\phi(\cdot)$ represents the embedding function parameterized by

ϕ . The rounding step translates the diffusion prediction in the embedding space back to discrete tokens: $p_\phi(\mathbf{y} \mid \mathbf{z}_0)$, whose parameter ϕ is shared with the embedding function. As a result, the neural network is trained end-to-end, optimizing both the reconstruction loss from the diffusion process and the consistency loss from the rounding step:

$$\mathcal{L} = \mathcal{L}_{reconstruct} + \underbrace{\mathbb{E}_{\mathbf{y}, \mathbf{z}_0} [-\log p_\phi(\mathbf{y} \mid \mathbf{z}_0)]}_{\mathcal{L}_{consistent}} \quad (7)$$

To control the generated data explicitly, we can introduce a guidance signal x to learn the conditional distribution $q(\mathbf{z} \mid x)$. A natural way is to supplement the conditioning information at each transition step during the original reverse process (Equation 3):

$$p_\theta(\mathbf{z}_0, \dots, \mathbf{z}_T \mid x) := p(\mathbf{z}_T) \prod_{t=1}^T p_\theta(\mathbf{z}_{t-1} \mid \mathbf{z}_t, x) \quad (8)$$

The unconditional model $\hat{\mathbf{z}}_\theta(\mathbf{z}_t, t)$ is replaced with the conditional model $\hat{\mathbf{z}}_\theta(\mathbf{z}_t, t, x)$, while the diffusion process remains unchanged. In MobilityGen, the guidance signal is derived from the traveled mobility events \mathbf{x} , and the model learns to generate a new target sequence \mathbf{y} based on this signal (Figure 1).

Neural network architecture

The neural network comprises several components: an embedding module that maps activity attributes into an embedding space, an encoder that extracts information from traveled traces, a decoder that reconstructs target sequences from their corrupted versions, and task-specific linear heads that ensure consistency mapping.

Inputs and embedding modules. The embedding process converts raw activity attributes of various formats into latent space representations. For categorical attributes with discrete values, such as the location identifier l and travel mode m , we introduce lookup matrices \mathcal{E}_l and \mathcal{E}_m that map attributes to the embedding space, $\mathcal{E}_l : \mathcal{V}_l \rightarrow \mathbb{R}^{d_{emb}}$ and $\mathcal{E}_m : \mathcal{V}_m \rightarrow \mathbb{R}^{d_{emb}}$, where \mathcal{V} represents the set of possible values and d_{emb} denotes the number of hidden dimensions. Intuitively, each row in \mathcal{E} corresponds to the representation of a specific value. For continuous attributes, such as the start time t and duration d , we use small feed-forward networks f_t and f_d to map the value into the hidden space, $f_t : \mathbb{R}^1 \rightarrow \mathbb{R}^{d_{emb}}$ and $f_d : \mathbb{R}^1 \rightarrow \mathbb{R}^{d_{emb}}$. The representation for an event record y_i in the target sequence is obtained by linearly combining the above-introduced transformations:

$$\mathbf{e}_\phi(y_i) = \mathcal{E}_l(l_i) + \mathcal{E}_m(m_i) + f_t(t_i) + f_d(d_i) \quad (9)$$

For each record x_k in the traveled sequence, we also incorporate the geometry g_k and surrounding land-use functions c_k . The geometry is modeled using the Space2vec method [63], which transforms raw coordinates in a projected coordinate system into vector representations via sine and cosine base functions. Land-use functions are captured using the location-POI embedding method proposed by Hong et al. [46], which considers POIs from various categories within a location and applies Latent Dirichlet Allocation (LDA) to derive their functional descriptions. The relationships between these movement-related contexts and the activity embeddings are learned through feed-forward networks f and linearly combined via a residual connection:

$$\mathbf{e}_\phi(x_k) = \mathbf{h}(x_k) + f_{coord}(s2v(g_k) \oplus \mathbf{h}(x_k)) + f_{poi}(lda(c_k) \oplus \mathbf{h}(x_k)) \quad (10)$$

$$\text{with } \mathbf{h}(x_k) = \mathcal{E}_l(l_k) + \mathcal{E}_m(m_k) + f_t(t_k) + f_d(d_k) \quad (11)$$

where \oplus denotes the concatenation operation. The final traveled sequence representation $\mathbf{e}_\phi(\mathbf{x})$ and target sequence representation $\mathbf{e}_\phi(\mathbf{y})$ consist of concatenated activity records in their sequential order. The parameters involved in the embedding process are optimized during network training.

Encoder and decoder design. We utilize the transformer encoder-decoder architecture proposed by Vaswani et al. [26]. The encoder processes the traveled sequence representation through L encoder blocks, each with an identical architecture consisting of a multi-head self-attention layer and a feed-forward layer with two linear operations separated by a non-linear activation function. Residual connections [64], layer normalizations [65], and dropout [66] are applied to each layer. The decoder, which processes the corrupted target sequence representation, contains L decoder blocks structured similarly to the encoder. In addition to the two layers in each encoder block, the decoder incorporates an intermediate layer that performs multi-head attention over the encoder stack’s output.

The multi-head attention layer consists of multiple attention operations, each computing an output from a query and a set of key-value pairs. In this context, the query, key, and value are vectors with the same dimension, denoted as d_{model} . Vaswani et al. [26] introduced scaled dot-product attention, which is efficiently implemented by packing sets of query, key, and value vectors into matrices \mathbf{Q} , \mathbf{K} , and \mathbf{V} , respectively:

$$\text{Attention}(\mathbf{Q}, \mathbf{K}, \mathbf{V}) = \text{softmax}\left(\frac{\mathbf{Q}\mathbf{K}^T}{\sqrt{d_{model}}}\right) \cdot \mathbf{V} \quad (12)$$

Multi-head attention is constructed by scaling the matrices \mathbf{Q} , \mathbf{K} , and \mathbf{V} across H attention operations

and concatenating their results:

$$\text{MultiHead}(\mathbf{Q}, \mathbf{K}, \mathbf{V}) = (\text{head}_1 \oplus \dots \oplus \text{head}_H) \cdot \mathbf{W}^O \quad (13)$$

$$\text{with } \text{head}_i = \text{Attention}(\mathbf{Q}\mathbf{W}_i^Q, \mathbf{K}\mathbf{W}_i^K, \mathbf{V}\mathbf{W}_i^V) \quad (14)$$

where \mathbf{W} denotes parameter matrices optimized during network training. In the decoder’s multi-head attention layers, the queries are derived from the previous decoder block, while the keys and values come from the encoder stack’s output. In the self-attention layers of both the encoder and decoder, the keys, values, and queries are all set to the output of the previous block. Additionally, causal masks are applied in the decoder’s self-attention operations to prevent access to information from “future” time steps, i.e., the entry at step k can only attend to information from step k and earlier. Ultimately, the encoder extracts the feature representation x from the traveled mobility sequence, which is then used in the decoder to reconstruct the target trace representation $\hat{\mathbf{z}}_\theta(\mathbf{z}_t, t, x)$.

Output heads and training objectives. Since we aim to generate new multifaceted activity events, the neural network must include multiple task-specific heads in the rounding step to “translate” from the embedding space into respective activity attributes. We introduce linear feed-forward layers $g_l : \mathbb{R}^{d_{emb}} \rightarrow \mathbb{R}^{|\mathcal{V}_l|}$, $g_m : \mathbb{R}^{d_{emb}} \rightarrow \mathbb{R}^{|\mathcal{V}_m|}$, $g_t : \mathbb{R}^{d_{emb}} \rightarrow \mathbb{R}^1$, and $g_d : \mathbb{R}^{d_{emb}} \rightarrow \mathbb{R}^1$ for directly mapping to location identifier, travel mode, start time, and duration, respectively.

The parameters of g_l and g_m are tied to the corresponding embedding modules, and their outputs are processed with a softmax operation to ensure a valid probability distribution over the set of possible values:

$$P(\hat{\mathbf{l}}) = \text{softmax}(g_l(\mathbf{z}_0)) \quad P(\hat{\mathbf{m}}) = \text{softmax}(g_m(\mathbf{z}_0)) \quad (15)$$

where $P(\hat{\mathbf{l}}) \in \mathbb{R}^{n \times |\mathcal{V}_l|}$ and $P(\hat{\mathbf{m}}) \in \mathbb{R}^{n \times |\mathcal{V}_m|}$ matrices contain the predicted probabilities for all locations and travel modes, respectively. The rounding errors are measured as the average of multi-class cross-entropy loss across the sequence:

$$\mathcal{L}_l = -\frac{1}{n} \sum_{i=1}^n \sum_{j=1}^{|\mathcal{V}_l|} P(\mathbf{l})_{[i,j]} \log(P(\hat{\mathbf{l}})_{[i,j]}) \quad \mathcal{L}_m = -\frac{1}{n} \sum_{i=1}^n \sum_{j=1}^{|\mathcal{V}_m|} P(\mathbf{m})_{[i,j]} \log(P(\hat{\mathbf{m}})_{[i,j]}) \quad (16)$$

where $P(\cdot)_{[i,j]}$ extracts the value at row i and column j , and $P(\mathbf{l})$ and $P(\mathbf{m})$ are the one-hot represented ground truth, e.g., $P(\mathbf{l})_{[i,j]} = 1$ if the chosen location at step i is the j^{th} location, and $P(\mathbf{l})_{[i,j]} = 0$ otherwise.

The rounding losses for start time and duration are measured directly as the mean squared error after the linear heads:

$$\mathcal{L}_t = \|g_s(\mathbf{z}_0) - \mathbf{s}\|^2 \quad \mathcal{L}_d = \|g_d(\mathbf{z}_0) - \mathbf{d}\|^2 \quad (17)$$

Finally, we obtain the consistency loss $\mathcal{L}_{consistent}$ by combining the task-specific rounding losses:

$$\mathcal{L}_{consistent} = \alpha_1 \mathcal{L}_l + \alpha_2 \mathcal{L}_m + \alpha_3 \mathcal{L}_t + \alpha_4 \mathcal{L}_d \quad (18)$$

where α values are weights that balance the contributions of the individual losses.

Training procedure and computational cost

We optimize the network parameters with Eq. 7 on the training set using the AdamW variant of stochastic gradient descent [67], employing a weight decay of 0.01 and an adaptive learning rate that starts at $4e^{-4}$ and is progressively reduced to $2e^{-5}$ following a cosine schedule. Training is conducted over 250,000 steps, with a batch size of 64 traveled-target sequence pairs per step (approximately 32,000 tokens). A linear learning rate warm-up [26] is applied for the first 5,000 steps. To stabilize training, we first optimize the network for 100,000 steps using only the \mathcal{L}_l loss, setting $\alpha_1 = 1$, and $\alpha_2 = \alpha_3 = \alpha_4 = 0$. For the remaining steps, we apply the efficient multiple-gradient descent algorithm for encoder-decoder architectures [68] to dynamically adjust the α values, ensuring the parameter optimization process leads to a Pareto optimal solution, where no task can be improved without compromising at least one of the others. We use the *sqrt* noise schedule [61] to determine the injected noise β_t at each forward diffusion step and apply loss-weighted sampling to select the noise steps t during training [62]. The transformer encoder and decoder each contain $L = 6$ blocks and $H = 8$ heads per attention layer. We set the forward diffusion steps to $T = 2000$, latent embedding size to $d_{emb} = 128$, and the transformer model representation size to $d_{model} = 512$. These hyperparameters were determined through a random search, selecting the best-performing set that minimized the network loss on the validation set.

The complete training process takes ≈ 82 hours using distributed data parallelism across four NVIDIA 4090 GPUs with FP16 half-precision. During inference, we down-sample the diffusion steps to $T = 200$ and allow the model to generate target sequences of length $n = 50$ steps, which, on average, correspond to 12.7 days of activity events. Generating a new target sequence takes 50.4 ± 4.1 milliseconds on a single NVIDIA 3090 GPU.

Evaluation metrics for mobility modeling

We use metrics that summarize high-level mobility patterns at collective and individual levels to quantify the discrepancy between ground truth and generated activity sequences. Here, we consider the following indicators:

- Location visitation frequency [8, 17]. Individuals’ preferences in location choices are highly unbalanced and can be quantified by the relationship between the visitation frequency of locations f_k and their rank k , which is reported to follow Zipf’s law, i.e., $f_k \sim k^{-\xi}$, with $\xi \sim 1.2$.
- Evolution of radius of gyration [8, 16]. The radius of gyration r_u measures the characteristic distance traveled by individual u and is used to reflect mobility intensity in the spatial dimension. Its evolution after k displacements $r_u(k)$ is defined as:

$$r_u(k) = \sqrt{\frac{1}{k} \sum_{i=1}^k (l^{(i)} - l_u^{cm})^2}$$

where $l^{(i)}$ represents the position of the i^{th} visited location, and $l_u^{cm} = \frac{1}{k} \sum_{j=1}^k l^{(j)}$ is the center of mass of the location sequence after k displacements.

- Temporal mobility entropy [11]. Closely related to the theoretical predictability of location sequences, temporal mobility entropy S_{temp} captures the full spatio-temporal order of location visits by measuring the probability $P(T'_u)$ of observing ordered subsequences T'_u within the location sequence T_u :

$$S_{temp} = - \sum_{T'_u \in T_u} P(T'_u) \log_2(P(T'_u))$$

We use the method described in Song et al. [11] to estimate the temporal mobility entropy S_{temp} for individuals.

- Mobility motifs [41]. Mobility motifs refer to recurring network patterns that emerge when daily location visits are abstracted as networks, where nodes represent activity locations and links denote transitions between them. We segmented the activity events by day and identified motif structures as those occurring in more than 0.5% of all days. The construction of these motifs incorporates both spatial and temporal dimensions of activity participation. Mobility regularity is quantified by the presence and frequency of specific motifs in individuals’ schedules [33].

- Evolution of trip package choices [43]. The trip package concept was introduced to encapsulate the interactions within multifaceted activity-travel patterns. For each individual, a trip package is constructed when observing the usage of a travel mode to reach an activity location, i.e., a unique mode-location choice. Individuals continuously explore new activity-behavior options, and the number of unique trip packages observed over time quantifies the speed of this exploratory behavior.

Identifying urban functions from POI features

POIs reflect the socioeconomic activities in local regions and have been increasingly used to identify urban functions at a fine scale [48]. A well-established approach to functional identification involves obtaining a POI representation for each study unit, identifying cluster structures from these representations, and labeling the resulting classes based on expert knowledge [49]. Here, we perform k -means clustering on the LDA functional descriptor of each location. Using the silhouette score to assess clustering quality, we determine the optimal number of classes to be five (Extended Data Figure 3a). Visualizing the five-class clustering result using 2-dimensional t-SNE reveals that the data points within each class are compact, while those between classes are well-separated (Extended Data Figure 3b). To interpret the urban functions of each location group, we rely on the spatial distribution of classes (Extended Data Figure 3c) and the POI enrichment factor for each class (Extended Data Table 5). The latter quantifies the relative occurrence of different categories of POIs. For each location class i and POI category q , the enrichment factor EF_i^q is defined as:

$$EF_i^q = \frac{N_i^q/N_i}{N^q/N}$$

where N_i^q represents the number of category q POIs in location class i , N_i denotes the total number of POIs in location class i , N^q indicates the total number of category q POIs, and N signifies the total number of POIs in the study area.

We label Cluster 0 as the *City center* due to its high prevalence in urban areas and the significant frequency of catering, health, and monetary-related POIs. Locations in Cluster 1 are dispersed outside the city and exhibit a high density of public facilities, leading to their classification as *Residential & Countryside*. Clusters 2 and 3 are designated as *Leisure & Recreation* and *Nature & Tourism*, respectively, due to their notable concentrations of leisure and nature-related POIs. Lastly, locations in Cluster 4 are typically situated near Cluster 0, and given their relatively even distribution of POIs, we classify this cluster as *Suburbs & Developing areas*.

The identification of urban functions is based on the locations' LDA functional descriptors, which are

the same data as employed by MobilityGen. Since the process primarily relies on the structure of the data itself, we believe that this result offers a direct illustration of the information used in MobilityGen.

Deriving experienced income segregation

To measure income segregation, we divide individuals into four roughly equal-sized quartiles according to their reported monthly household income: low ($< 4,000$ CHF), lower-middle ($4,000 - 8,000$ CHF), upper-middle ($8,000 - 12,000$ CHF), and high ($> 12,000$ CHF). We then apply the experienced income segregation framework introduced by Moro et al. [34], described in detail below.

At the location level, segregation is computed from the proportion of time individuals in income quartile q spend at each location l , denoted by τ_{ql} . Assuming that a fully integrated location corresponds to an equal distribution of time spent across quartiles (i.e., $\tau_{ql} = \frac{1}{4}$), the location-level segregation score S_l is defined as: $S_l = \frac{2}{3} \sum_q \left| \tau_{ql} - \frac{1}{4} \right|$. This score, ranging from 0 (perfect integration) to 1 (complete segregation), quantifies the imbalance in visitation by income groups.

To measure segregation at the individual level, we calculate each person’s relative exposure to income quartiles based on the locations they visit. Let τ_{ul} represent the proportion of time individual u spends at location l . Their exposure to quartile q , denoted by τ_{uq} , is then: $\tau_{uq} = \sum_l \tau_{ul} \tau_{ql}$. Using this, the individual-level segregation score S_u is defined analogously to the location-level score:

$$S_u = \frac{2}{3} \sum_q \left| \tau_{uq} - \frac{1}{4} \right|$$

As with S_l , a score of $S_u = 0$ indicates perfectly balanced exposure across income groups, while $S_u = 1$ reflects exclusive exposure to a single group.

This formulation approximates co-presence by averaging the time spent at each location across income groups, rather than relying on exact co-occurrence events. As such events are extremely sparse in real mobility data, this time-invariant approach provides a practical way to estimate individual-level interaction patterns. We compute individual-level income segregation scores for each real and simulated event sequence in the testing set. Since multiple sequences may originate from the same individual (and thus the same income group), and often involve repeated visits to similar locations, the resulting scores do not reflect population-wide segregation within the study area. Instead, they serve as a validation metric to assess how well MobilityGen reproduces the co-presence patterns observed in the real data.

References

- [1] K. W. Axhausen, T. Gärling, Activity-based approaches to travel analysis: conceptual frameworks, models, and research problems, *Transport Reviews* 12 (1992) 323–341. doi:doi:10.1080/01441649208716826.
- [2] S. Burbidge, K. Goulias, Active travel behavior, *Transportation letters* 1 (2009) 147–167. doi:doi:10.3328/TL.2009.01.02.147-167.
- [3] S. Hanson, P. Hanson, The travel-activity patterns of urban residents: dimensions and relationships to sociodemographic characteristics, *Economic geography* 57 (1981) 332–347. doi:doi:10.2307/144213.
- [4] B. Jiang, J. Yin, S. Zhao, Characterizing the human mobility pattern in a large street network, *Physical Review E—Statistical, Nonlinear, and Soft Matter Physics* 80 (2009) 021136. doi:doi:10.1103/PhysRevE.80.021136.
- [5] S. L. Handy, M. G. Boarnet, R. Ewing, R. E. Killingsworth, How the built environment affects physical activity: views from urban planning, *American journal of preventive medicine* 23 (2002) 64–73. doi:doi:10.1016/S0749-3797(02)00475-0.
- [6] J. Hong, Q. Shen, L. Zhang, How do built-environment factors affect travel behavior? a spatial analysis at different geographic scales, *Transportation* 41 (2014) 419–440. doi:doi:10.1007/s11116-013-9462-9.
- [7] D. Brockmann, L. Hufnagel, T. Geisel, The scaling laws of human travel, *Nature* 439 (2006) 462–465. doi:doi:10.1038/nature04292.
- [8] M. C. González, C. A. Hidalgo, A.-L. Barabási, Understanding individual human mobility patterns, *Nature* 453 (2008) 779–782. doi:doi:10.1038/nature06958.
- [9] L. Alessandretti, P. Sapiezynski, V. Sekara, S. Lehmann, A. Baronchelli, Evidence for a conserved quantity in human mobility, *Nature Human Behaviour* 2 (2018) 485–491. doi:doi:10.1038/s41562-018-0364-x.
- [10] M. Schlöpfer, L. Dong, K. O’Keeffe, P. Santi, M. Szell, H. Salat, S. Anklesaria, M. Vazifeh, C. Ratti, G. B. West, The universal visitation law of human mobility, *Nature* 593 (2021) 522–527. doi:doi:10.1038/s41586-021-03480-9.
- [11] C. Song, Z. Qu, N. Blumm, A.-L. Barabasi, Limits of Predictability in Human Mobility, *Science* 327 (2010) 1018–1021. doi:doi:10.1126/science.1177170.
- [12] S. Hörl, M. Balac, Synthetic population and travel demand for Paris and Île-de-France based on open and publicly available data, *Transportation Research Part C: Emerging Technologies* 130 (2021) 103291. doi:doi:10.1016/j.trc.2021.103291.
- [13] J. Pougala, T. Hillel, M. Bierlaire, OASIS: Optimisation-based Activity Scheduling with Integrated Simultaneous choice dimensions, *Transportation Research Part C: Emerging Technologies* 155 (2023) 104291. doi:doi:10.1016/j.trc.2023.104291.
- [14] C. R. Bhat, S. K. Singh, A comprehensive daily activity-travel generation model system for workers, *Transportation Research Part A: Policy and Practice* 34 (2000) 1–22. doi:doi:10.1016/S0965-8564(98)00037-8.
- [15] J. Auld, A. K. Mohammadian, Activity planning processes in the Agent-based Dynamic Activity Planning and Travel Scheduling (ADAPTS) model, *Transportation Research Part A: Policy and Practice* 46 (2012) 1386–1403. doi:doi:10.1016/j.tra.2012.05.017.
- [16] L. Alessandretti, U. Aslak, S. Lehmann, The scales of human mobility, *Nature* 587 (2020) 402–407. doi:doi:10.1038/s41586-020-2909-1.
- [17] C. Song, T. Koren, P. Wang, A.-L. Barabási, Modelling the scaling properties of human mobility, *Nature Physics* 6 (2010) 818–823. doi:doi:10.1038/nphys1760.
- [18] L. Pappalardo, F. Simini, S. Rinzivillo, D. Pedreschi, F. Giannotti, A.-L. Barabási, Returners and explorers dichotomy in human mobility, *Nature Communications* 6 (2015) 8166. doi:doi:10.1038/ncomms9166.

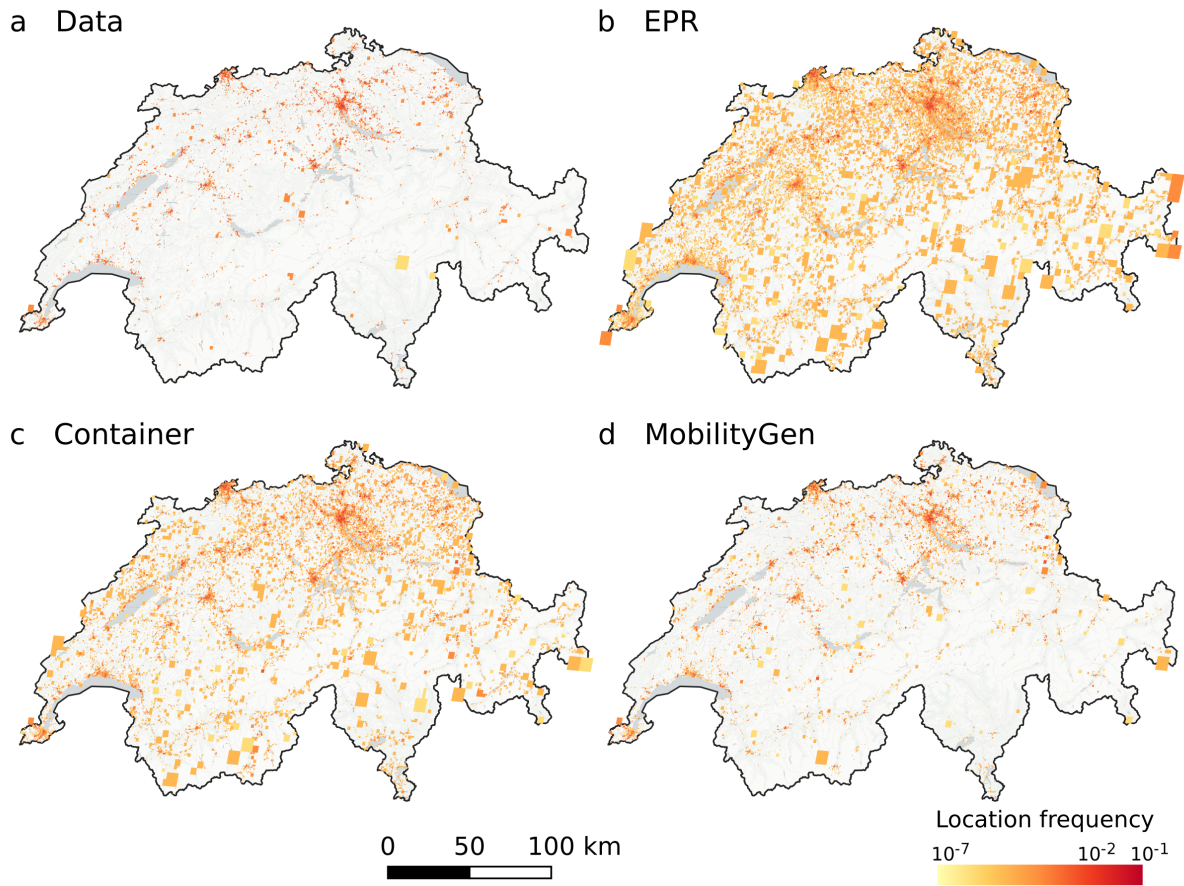
- [19] H. Barbosa, F. B. de Lima-Neto, A. Evsukoff, R. Menezes, The effect of recency to human mobility, *EPJ Data Science* 4 (2015) 21. doi:doi:[10.1140/epjds/s13688-015-0059-8](https://doi.org/10.1140/epjds/s13688-015-0059-8).
- [20] C. Zhao, A. Zeng, C. H. Yeung, Characteristics of human mobility patterns revealed by high-frequency cell-phone position data, *EPJ Data Science* 10 (2021) 1–14. doi:doi:[10.1140/epjds/s13688-021-00261-2](https://doi.org/10.1140/epjds/s13688-021-00261-2).
- [21] L. Pappalardo, E. Manley, V. Sekara, L. Alessandretti, Future directions in human mobility science, *Nature Computational Science* 3 (2023) 588–600. doi:doi:[10.1038/s43588-023-00469-4](https://doi.org/10.1038/s43588-023-00469-4).
- [22] Y. Xu, S. Çolak, E. C. Kara, S. J. Moura, M. C. González, Planning for electric vehicle needs by coupling charging profiles with urban mobility, *Nature Energy* 3 (2018) 484–493. doi:doi:[10.1038/s41560-018-0136-x](https://doi.org/10.1038/s41560-018-0136-x).
- [23] S. Zhang, F. Zhen, Y. Kong, T. Lobsang, S. Zou, Towards a 15-minute city: A network-based evaluation framework, *Environment and Planning B: Urban Analytics and City Science* 50 (2023) 500–514. doi:doi:[10.1177/23998083221118570](https://doi.org/10.1177/23998083221118570).
- [24] F. Barreras, D. J. Watts, The exciting potential and daunting challenge of using GPS human-mobility data for epidemic modeling, *Nature Computational Science* 4 (2024) 398–411. doi:doi:[10.1038/s43588-024-00637-0](https://doi.org/10.1038/s43588-024-00637-0).
- [25] Y. LeCun, Y. Bengio, G. Hinton, Deep learning, *Nature* 521 (2015) 436–444. doi:doi:[10.1038/nature14539](https://doi.org/10.1038/nature14539).
- [26] A. Vaswani, N. Shazeer, N. Parmar, J. Uszkoreit, L. Jones, A. N. Gomez, L. Kaiser, I. Polosukhin, Attention is all you need, in: *31st Conference on Neural Information Processing Systems (NIPS '17)*, 2017, pp. 5998–6008.
- [27] J. Sohl-Dickstein, E. Weiss, N. Maheswaranathan, S. Ganguli, Deep Unsupervised Learning using Nonequilibrium Thermodynamics, in: *Proceedings of the 32nd International Conference on Machine Learning (ICML '15)*, 2015, pp. 2256–2265.
- [28] J. Ho, A. Jain, P. Abbeel, Denoising diffusion probabilistic models, in: *34th Conference on Neural Information Processing Systems (NeurIPS '20)*, volume 33, Curran Associates, Inc., 2020, pp. 6840–6851.
- [29] Y. Liu, S. Wang, J. Dong, L. Chen, X. Wang, L. Wang, F. Li, C. Wang, J. Zhang, Y. Wang, S. Wei, Q. Chen, H. Liu, De novo protein design with a denoising diffusion network independent of pretrained structure prediction models, *Nature Methods* (2024) 1–10. doi:doi:[10.1038/s41592-024-02437-w](https://doi.org/10.1038/s41592-024-02437-w).
- [30] T. Li, L. Biferale, F. Bonaccorso, M. A. Scarpolini, M. Buzzicotti, Synthetic Lagrangian turbulence by generative diffusion models, *Nature Machine Intelligence* 6 (2024) 393–403. doi:doi:[10.1038/s42256-024-00810-0](https://doi.org/10.1038/s42256-024-00810-0).
- [31] G. Savcicens, T. Eliassi-Rad, L. K. Hansen, L. H. Mortensen, L. Lilleholt, A. Rogers, I. Zettler, S. Lehmann, Using sequences of life-events to predict human lives, *Nature Computational Science* 4 (2024) 43–56. doi:doi:[10.1038/s43588-023-00573-5](https://doi.org/10.1038/s43588-023-00573-5).
- [32] D. J. Reck, H. Martin, K. W. Axhausen, Mode choice, substitution patterns and environmental impacts of shared and personal micro-mobility, *Transportation Research Part D: Transport and Environment* 102 (2022) 103134. doi:doi:[10.1016/j.trd.2021.103134](https://doi.org/10.1016/j.trd.2021.103134).
- [33] S. Jiang, Y. Yang, S. Gupta, D. Veneziano, S. Athavale, M. C. González, The TimeGeo modeling framework for urban mobility without travel surveys, *Proceedings of the National Academy of Sciences* 113 (2016) E5370–E5378. doi:doi:[10.1073/pnas.1524261113](https://doi.org/10.1073/pnas.1524261113).
- [34] E. Moro, D. Calacci, X. Dong, A. Pentland, Mobility patterns are associated with experienced income segregation in large US cities, *Nature Communications* 12 (2021) 4633. doi:doi:[10.1038/s41467-021-24899-8](https://doi.org/10.1038/s41467-021-24899-8).
- [35] H. Nilforoshan, W. Looi, E. Pierson, B. Villanueva, N. Fishman, Y. Chen, J. Sholar, B. Redbird, D. Grusky, J. Leskovec, Human mobility networks reveal increased segregation in large cities, *Nature* 624 (2023) 586–592. doi:doi:[10.1038/s41586-023-06757-3](https://doi.org/10.1038/s41586-023-06757-3).
- [36] Z. Liu, C. Liu, A. Mostafavi, Beyond residence: A mobility-based approach for improved evaluation of human exposure

- to environmental hazards, *Environmental Science & Technology* 57 (2023) 15511–15522. doi:doi:[10.1021/acs.est.3c04691](https://doi.org/10.1021/acs.est.3c04691).
- [37] H. Barbosa, M. Barthelemy, G. Ghoshal, C. R. James, M. Lenormand, T. Louail, R. Menezes, J. J. Ramasco, F. Simini, M. Tomasini, Human mobility: Models and applications, *Physics Reports* 734 (2018) 1–74. doi:doi:[10.1016/j.physrep.2018.01.001](https://doi.org/10.1016/j.physrep.2018.01.001).
- [38] A. Clauset, C. R. Shalizi, M. E. Newman, Power-law distributions in empirical data, *SIAM review* 51 (2009) 661–703. doi:doi:[10.1137/070710111](https://doi.org/10.1137/070710111).
- [39] V. M. Panaretos, Y. Zemel, Statistical Aspects of Wasserstein Distances, *Annual Review of Statistics and Its Application* 6 (2019) 405–431. doi:doi:[10.1146/annurev-statistics-030718-104938](https://doi.org/10.1146/annurev-statistics-030718-104938).
- [40] A. Cuttone, Sune Lehmann, M. C. González, Understanding predictability and exploration in human mobility, *EPJ Data Science* 7 (2018) 2. doi:doi:[10.1140/epjds/s13688-017-0129-1](https://doi.org/10.1140/epjds/s13688-017-0129-1).
- [41] C. M. Schneider, V. Belik, T. Couronné, Z. Smoreda, M. C. González, Unravelling daily human mobility motifs, *Journal of The Royal Society Interface* 10 (2013) 20130246. doi:doi:[10.1098/rsif.2013.0246](https://doi.org/10.1098/rsif.2013.0246).
- [42] L. Pappalardo, F. Simini, Data-driven generation of spatio-temporal routines in human mobility, *Data Mining and Knowledge Discovery* 32 (2018) 787–829. doi:doi:[10.1007/s10618-017-0548-4](https://doi.org/10.1007/s10618-017-0548-4).
- [43] Y. Hong, H. Martin, Y. Xin, D. Bucher, D. J. Reck, K. W. Axhausen, M. Raubal, Conserved quantities in human mobility: From locations to trips, *Transportation Research Part C: Emerging Technologies* 146 (2023) 103979. doi:doi:[10.1016/j.trc.2022.103979](https://doi.org/10.1016/j.trc.2022.103979).
- [44] A. Narayan, B. Berger, H. Cho, Assessing single-cell transcriptomic variability through density-preserving data visualization, *Nature Biotechnology* 39 (2021) 765–774. doi:doi:[10.1038/s41587-020-00801-7](https://doi.org/10.1038/s41587-020-00801-7).
- [45] P. Zhao, H. Wang, Q. Liu, X.-Y. Yan, J. Li, Unravelling the spatial directionality of urban mobility, *Nature Communications* 15 (2024) 4507. doi:doi:[10.1038/s41467-024-48909-7](https://doi.org/10.1038/s41467-024-48909-7).
- [46] Y. Hong, Y. Zhang, K. Schindler, M. Raubal, Context-aware multi-head self-attentional neural network model for next location prediction, *Transportation Research Part C: Emerging Technologies* 156 (2023) 104315. doi:doi:[10.1016/j.trc.2023.104315](https://doi.org/10.1016/j.trc.2023.104315).
- [47] T. A. Arentze, H. J. P. Timmermans, Information gain, novelty seeking and travel: a model of dynamic activity-travel behavior under conditions of uncertainty, *Transportation Research Part A: Policy and Practice* 39 (2005) 125–145. doi:doi:[10.1016/j.tra.2004.08.002](https://doi.org/10.1016/j.tra.2004.08.002).
- [48] Y. Yao, X. Li, X. Liu, P. Liu, Z. Liang, J. Zhang, K. Mai, Sensing spatial distribution of urban land use by integrating points-of-interest and Google Word2Vec model, *International Journal of Geographical Information Science* 31 (2017) 825–848. doi:doi:[10.1080/13658816.2016.1244608](https://doi.org/10.1080/13658816.2016.1244608).
- [49] H. Niu, E. A. Silva, Delineating urban functional use from points of interest data with neural network embedding: A case study in Greater London, *Computers, Environment and Urban Systems* 88 (2021) 101651. doi:doi:[10.1016/j.compenvurbsys.2021.101651](https://doi.org/10.1016/j.compenvurbsys.2021.101651).
- [50] G. K. Zipf, The P1 P2/D Hypothesis: On the Intercity Movement of Persons, *American Sociological Review* 11 (1946) 677–686. doi:doi:[10.2307/2087063](https://doi.org/10.2307/2087063).
- [51] F. Simini, G. Barlacchi, M. Luca, L. Pappalardo, A Deep Gravity model for mobility flows generation, *Nature Communications* 12 (2021) 6576. doi:doi:[10.1038/s41467-021-26752-4](https://doi.org/10.1038/s41467-021-26752-4).
- [52] O. Cabanas-Tirapu, L. Danús, E. Moro, M. Sales-Pardo, R. Guimerà, Human mobility is well described by closed-form gravity-like models learned automatically from data, *Nature Communications* 16 (2025) 1336. doi:doi:[10.1038/s41467-025-](https://doi.org/10.1038/s41467-025-)

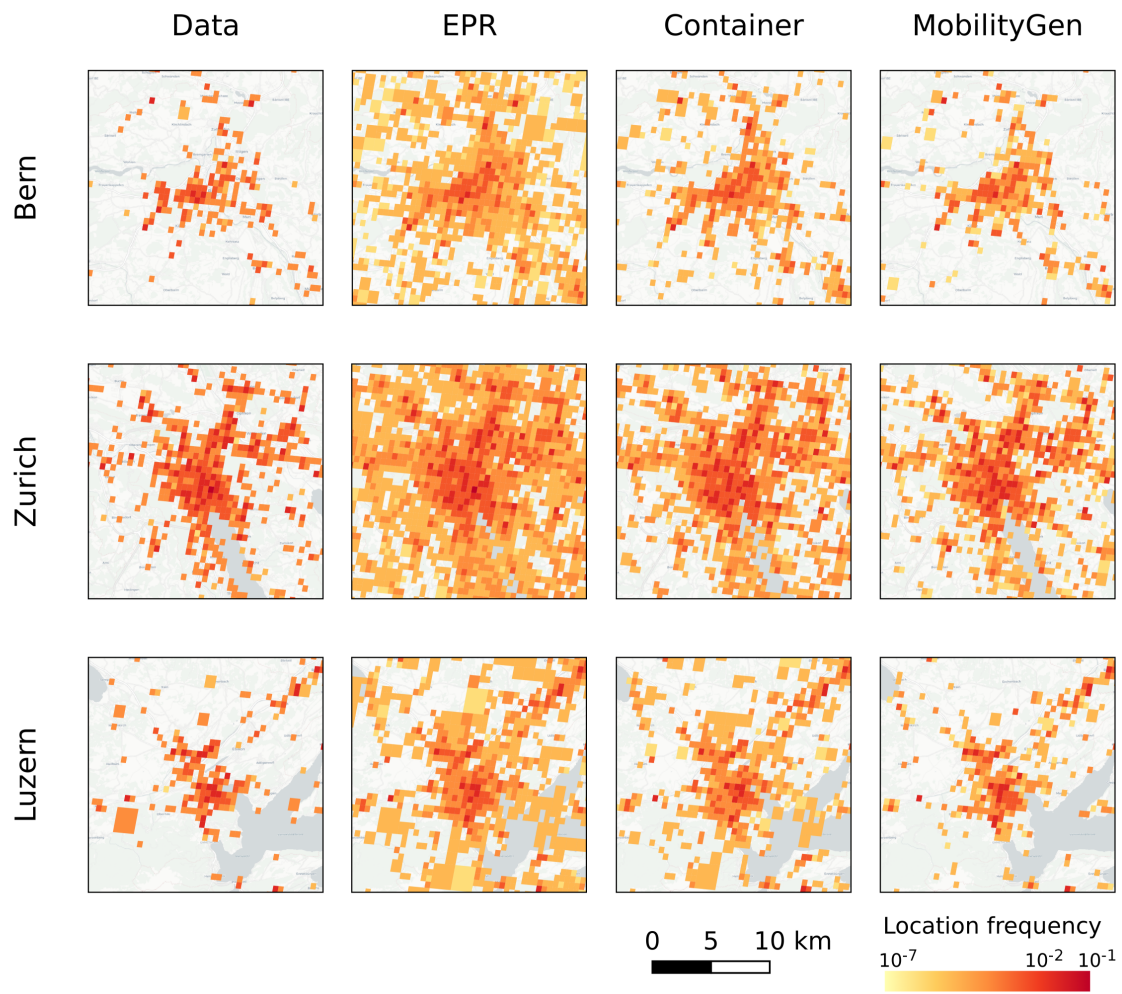
56495-5.

- [53] T. Abbasov, C. Heine, S. Sabouri, A. Salazar-Miranda, P. Santi, E. Glaeser, C. Ratti, The 15-minute city quantified using human mobility data, *Nature Human Behaviour* (2024). doi:doi:[10.1038/s41562-023-01770-y](https://doi.org/10.1038/s41562-023-01770-y).
- [54] Y. Liao, J. Gil, S. Yeh, R. H. Pereira, L. Alessandretti, Socio-spatial segregation and human mobility: A review of empirical evidence, *Computers, Environment and Urban Systems* 117 (2025) 102250. doi:doi:[10.1016/j.compenvurbsys.2025.102250](https://doi.org/10.1016/j.compenvurbsys.2025.102250).
- [55] J. Molloy, A. Castro, T. Götschi, B. Schoeman, C. Tchervenkov, U. Tomic, B. Hintermann, K. W. Axhausen, The MOBIS dataset: a large GPS dataset of mobility behaviour in Switzerland, *Transportation* 50 (2022) 1983–2007. doi:doi:[10.1007/s11116-022-10299-4](https://doi.org/10.1007/s11116-022-10299-4).
- [56] K. W. Axhausen, Definition of movement and activity for transport modelling, in: *Handbook of transport modelling*, Emerald Group Publishing Limited, 2007, pp. 329–343. doi:doi:[10.3929/ethz-a-005278091](https://doi.org/10.3929/ethz-a-005278091).
- [57] H. Martin, Y. Hong, N. Wiedemann, D. Bucher, M. Raubal, Trackintel: An open-source python library for human mobility analysis, *Computers, Environment and Urban Systems* 101 (2023) 101938. doi:doi:[10.1016/j.compenvurbsys.2023.101938](https://doi.org/10.1016/j.compenvurbsys.2023.101938).
- [58] C. Lu, Y. Zhou, F. Bao, J. Chen, C. Li, J. Zhu, DPM-Solver: A Fast ODE Solver for Diffusion Probabilistic Model Sampling in Around 10 Steps, in: *36th Conference on Neural Information Processing Systems (NeurIPS '22)*, Curran Associates, Inc., 2022, pp. 5775–5787.
- [59] L. Yang, Z. Zhang, Y. Song, S. Hong, R. Xu, Y. Zhao, W. Zhang, B. Cui, M.-H. Yang, Diffusion Models: A Comprehensive Survey of Methods and Applications, *ACM Computing Surveys* 56 (2023) 105:1–105:39. doi:doi:[10.1145/3626235](https://doi.org/10.1145/3626235).
- [60] J. Austin, D. D. Johnson, J. Ho, D. Tarlow, R. van den Berg, Structured denoising diffusion models in discrete state-spaces, in: *35th Conference on Neural Information Processing Systems (NeurIPS '21)*, 2021, pp. 17981–17993.
- [61] X. Li, J. Thickstun, I. Gulrajani, P. S. Liang, T. B. Hashimoto, Diffusion-LM Improves Controllable Text Generation, in: *36th Conference on Neural Information Processing Systems (NeurIPS '22)*, 2022, pp. 4328–4343.
- [62] S. Gong, M. Li, J. Feng, Z. Wu, L. Kong, DiffuSeq: Sequence to sequence text generation with diffusion models, in: *The 11th International Conference on Learning Representations (ICLR '23)*, 2023.
- [63] G. Mai, K. Janowicz, B. Yan, R. Zhu, L. Cai, N. Lao, Multi-Scale Representation Learning for Spatial Feature Distributions using Grid Cells, in: *8th International Conference on Learning Representations (ICLR '20)*, 2020.
- [64] K. He, X. Zhang, S. Ren, J. Sun, Deep residual learning for image recognition, in: *2016 IEEE Conference on Computer Vision and Pattern Recognition (CVPR '16)*, 2016, pp. 770–778. doi:doi:[10.1109/CVPR.2016.90](https://doi.org/10.1109/CVPR.2016.90).
- [65] J. L. Ba, J. R. Kiros, G. E. Hinton, Layer Normalization, 2016. doi:doi:[10.48550/arXiv.1607.06450](https://doi.org/10.48550/arXiv.1607.06450).
- [66] G. E. Hinton, N. Srivastava, A. Krizhevsky, I. Sutskever, R. R. Salakhutdinov, Improving neural networks by preventing co-adaptation of feature detectors, 2012. doi:doi:[10.48550/arXiv.1207.0580](https://doi.org/10.48550/arXiv.1207.0580).
- [67] I. Loshchilov, F. Hutter, Decoupled Weight Decay Regularization, in: *7th International Conference on Learning Representations (ICLR '19)*, 2019.
- [68] O. Sener, V. Koltun, Multi-task learning as multi-objective optimization, in: *32nd Conference on Neural Information Processing Systems (NeurIPS '18)*, 2018, pp. 525–536.
- [69] S. Gambs, M.-O. Killijian, M. N. del Prado Cortez, Next place prediction using mobility Markov chains, in: *Proceedings of the First Workshop on Measurement, Privacy, and Mobility (MPM '12)*, 2012, pp. 1–6. doi:doi:[10.1145/2181196.2181199](https://doi.org/10.1145/2181196.2181199).
- [70] J. Feng, Z. Yang, F. Xu, H. Yu, M. Wang, Y. Li, Learning to simulate human mobility, in: *26th ACM SIGKDD International Conference on Knowledge Discovery & Data Mining (KDD '20)*, 2020, pp. 3426 – 3433. doi:doi:[10.1145/3394486.341286](https://doi.org/10.1145/3394486.341286).

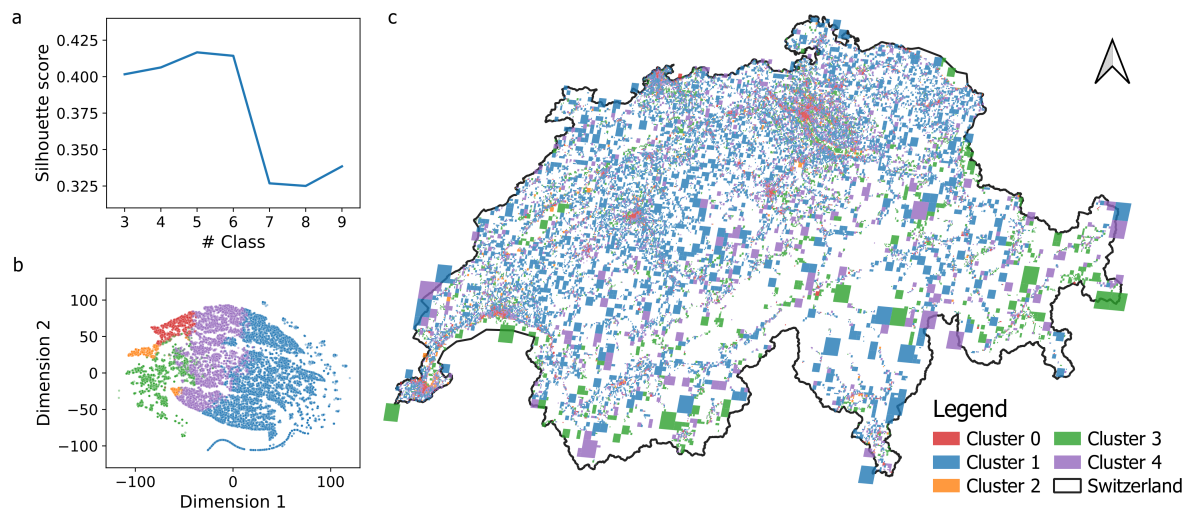
- [71] D. Ashbrook, T. Starner, Learning significant locations and predicting user movement with GPS, in: Proceedings of the 6th International Symposium on Wearable Computers (ISWC '02), 2002, pp. 101–108. doi:doi:[10.1109/ISWC.2002.1167224](https://doi.org/10.1109/ISWC.2002.1167224).
- [72] M. Luca, G. Barlacchi, B. Lepri, L. Pappalardo, A Survey on Deep Learning for Human Mobility, *ACM Computing Surveys* 55 (2021) 7:1–7:44. doi:doi:[10.1145/3485125](https://doi.org/10.1145/3485125).
- [73] A. Holtzman, J. Buys, L. Du, M. Forbes, Y. Choi, The Curious Case of Neural Text Degeneration, in: 8th International Conference on Learning Representations (ICLR '20), 2020.
- [74] K. Papineni, S. Roukos, T. Ward, W. Zhu, Bleu: a method for automatic evaluation of machine translation, in: Proceedings of the 40th Annual Meeting of the Association for Computational Linguistics (ACL '02), 2002, pp. 311–318. doi:doi:[10.3115/1073083.1073135](https://doi.org/10.3115/1073083.1073135).
- [75] A. Deshpande, J. Aneja, L. Wang, A. G. Schwing, D. A. Forsyth, Fast, diverse and accurate image captioning guided by part-of-speech, in: 2019 IEEE Conference on Computer Vision and Pattern Recognition (CVPR '19), 2019, pp. 10695–10704. doi:doi:[10.1109/CVPR.2019.01095](https://doi.org/10.1109/CVPR.2019.01095).
- [76] L. McInnes, J. Healy, N. Saul, L. Grossberger, Umap: Uniform manifold approximation and projection, *The Journal of Open Source Software* 3 (2018) 861. doi:doi:[10.21105/joss.00861](https://doi.org/10.21105/joss.00861).
- [77] F. Pedregosa, G. Varoquaux, A. Gramfort, V. Michel, B. Thirion, O. Grisel, M. Blondel, P. Prettenhofer, R. Weiss, V. Dubourg, J. Vanderplas, A. Passos, D. Cournapeau, M. Brucher, M. Perrot, E. Duchesnay, Scikit-learn: Machine learning in Python, *Journal of Machine Learning Research* 12 (2011) 2825–2830.



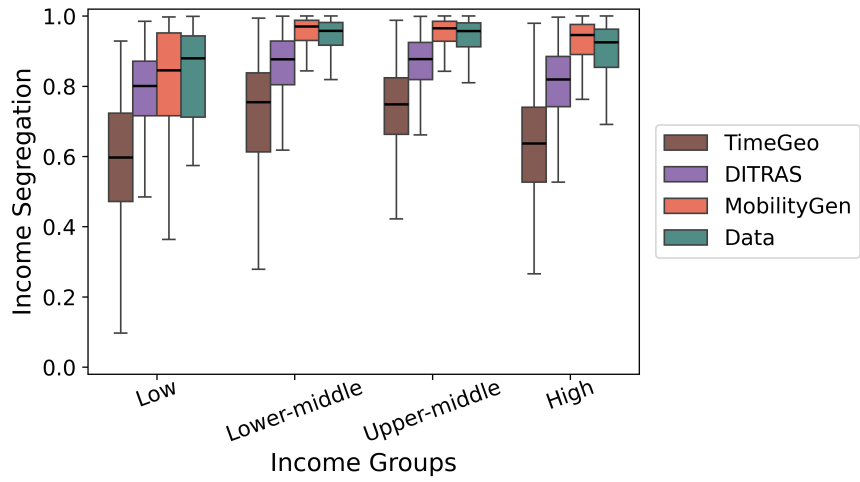
Extended Data Figure 1: Comparison of spatial visitation patterns across models. Aggregated visit frequencies from real data (a) are compared with those generated by three baseline mobility models: EPR (b), Container (c), and MobilityGen (d). While all models recover broad national-scale trends, MobilityGen more accurately reproduces both high-density urban visitation and spatial dispersion into surrounding regions.



Extended Data Figure 2: Urban-level comparison of spatial visitation patterns across models. Real and simulated visit frequencies are compared across Bern (top row), Zurich (middle row), and Lucerne (bottom row). Consistent with national-level patterns, MobilityGen best captures fine-grained spatial visitation within dense urban cores and across peripheral areas.



Extended Data Figure 3: Identifying urban functions using location LDA vectors and k -means clustering. **a**. The silhouette score assesses clustering quality, with higher values indicating more compact and better-separated classes. The score suggests that five classes yield the best separation. **b**. Clustering results visualized using 2D t-SNE, where each point represents a location, color-coded by class. **c**. Spatial distribution of the identified location classes, using the same color scheme as in **b**.



Extended Data Figure 4: Variation in income segregation across groups. Boxplots of individual-level income segregation scores for four income groups (low, lower-middle, upper-middle, and high), comparing observed data (teal) with sequences generated by TimeGeo (brown), DITRAS (purple), and MobilityGen (red). MobilityGen closely reproduces the empirical distributions and outperforms the baseline simulators in capturing variation in segregation levels across groups.

Extended Data Table 1: Model performance in replicating location visit distributions. The log-likelihood ratio measures the likelihood that the real data was generated by each model relative to MobilityGen, with positive values favoring MobilityGen (all $P < 10^{-3}$). The Wasserstein distance assesses the dissimilarity between generated and real location metric distributions, with higher values indicating greater divergence. Results are shown for number of visits per location (f_k) and temporal entropy (S_{temp}); best-performing values are shown in bold.

	Log-likelihood		Wasserstein distance	
	$P(f_k)$	$P(S_{\text{temp}})$	f_k	S_{temp}
EPR	114195	30298	2.62	0.54
Container	12504	3549	0.68	0.18
Markov	796846	2728649	2.03	0.73
MHSA	66983	9616	0.85	0.30
MovSim	268850	22837	5.04	0.51
MobilityGen (Ours)	-	-	0.26	0.04

Extended Data Table 2: Spatial dispersion in visitation patterns. Entropy values are reported for the real data and for location traces generated by each microscopic mobility model. Higher entropy indicates broader spatial dispersion of visits. Values below those of the real data suggest insufficient reproduction of exploratory behavior, while values above indicate misalignment with population-level location preferences.

	Study area	Bern	Zurich	Luzern
EPR	1.20	3.89	5.04	3.50
Container	0.91	3.13	4.60	3.18
Markov	0.17	1.03	2.07	1.34
MHSA	0.50	2.79	4.05	2.62
MovSim	0.67	3.21	4.30	2.58
MobilityGen (Ours)	0.53	2.49	3.99	2.71
Data	0.33	1.89	3.37	2.11

Extended Data Table 3: Alignment of behavioral patterns and interdependencies. The Wasserstein distance quantifies dissimilarities between metric distributions derived from simulated and real activity events, with higher values indicating greater divergence. Source sequence results are included as a reference baseline. Results are reported for activity duration (f_d), daily visited locations (f_k^{day}), mobility motifs (f_{motifs}), and travel mode (f_m); best-performing values are shown in bold.

	f_d	f_k^{day}	f_{motifs}	f_m
DITRAS	2.23	1.34	0.24	-
TimeGeo	1.96	1.59	1.73	-
MobilityGen (Ours)	0.47	0.29	0.14	0.048
Source sequence	0.58	0.66	0.27	0.043

Extended Data Table 4: Reconstructing mobility flows at novel locations. Simulated flows are compared with real flows at locations not seen during training. For MobilityGen, individual sequences are aggregated into an origin-destination matrix to enable comparison with flow-based models. Evaluation metrics include the common part of commuters (CPC), Pearson correlation coefficient (Pearson r), and Jensen-Shannon divergence (JSD). Arrows indicate the preferred direction for each metric. Entropy quantifies the spatial dispersion of visits to novel locations. Best-performing values are shown in bold.

	CPC \uparrow	Pearson r \uparrow	JSD \downarrow	Entropy
Gravity power-law	0.02	0.19	0.81	9.88
Random Forest	0.02	0.17	0.79	8.75
Deep Gravity	0.08	0.25	0.77	8.33
MobilityGen (Ours)	0.22	0.47	0.69	7.16
Data				6.92

Extended Data Table 5: POI enrichment across functional clusters. First-level POI categories with more than 1,000 instances in the study area were considered. For each cluster, the top three POI types with enrichment factors greater than 1 are highlighted in bold.

POI category	Cluster 0	Cluster 1	Cluster 2	Cluster 3	Cluster 4
Accommodation	1.28	0.90	0.41	0.92	0.97
Catering	1.88	0.71	0.44	0.43	0.82
Health	2.31	0.46	0.12	0.04	0.85
Leisure	0.48	1.22	3.26	0.28	1.08
Money	2.21	0.56	0.04	0.06	0.82
Natural	0.04	0.86	0.14	7.15	0.87
Others	1.01	0.83	0.87	1.81	1.03
Place of worships	0.56	1.68	0.22	0.32	0.85
Public	0.90	1.26	0.66	0.13	0.99
Shopping	1.59	0.83	0.37	0.31	0.92
Tourism	0.54	1.05	0.55	3.08	0.97
Traffic	1.00	1.09	0.64	0.50	1.02

Supplementary Note 1. Simulating individual preferences in location visits

Supplementary Note 1.1. Comparison with microscopic mobility models

To evaluate the ability of MobilityGen to replicate fundamental properties of individual location behavior, we compare it with representative microscopic mobility models spanning mechanistic, predictive, and generative approaches. These include: (i) classical mechanistic models such as the exploration and preferential return (EPR) model [17] and the Container model [16]; (ii) sequence prediction models, including a first-order Markov chain [69] and a multi-head self-attention (MHSA)-based neural network [46]; and (iii) the deep generative MoveSim model [70]. The design and implementation details of each model are described in the following sections.

- The EPR model is a well-established microscopic mobility model designed to reproduce scaling laws in the evolution of distinct locations and their visitation frequencies over time. We estimate model parameters from the training data. For each test sequence, we determine the number of unique locations S visited and the corresponding visit counts f_i for each location i , and then simulate 50 displacement steps. At each step, the individual either explores a new location with probability $p^{\text{new}} = \rho S^{-\gamma}$, where ρ and γ are parameters, or returns to a previously visited location with the complementary probability $1 - p^{\text{new}}$. In exploration steps, a new location is determined by sampling a displacement Δr from the empirically estimated jump length distribution $P(\Delta r)$. For return steps, the probability of selecting location j , denoted as Π_j , is proportional to its past visitation frequency, i.e., $\Pi_j \propto f_j$.
- Container model. Alessandretti et al. [16] introduced the Container model to describe how individuals allocate time and move across nested spatial scales. The model is built on a hierarchical structure H with L levels, where each level groups locations into increasingly broader spatial containers. Each container is associated with an attractiveness score a , and mobility decisions are governed by an $L \times L$ displacement matrix D . The probability of moving from the current location j to a destination k is given by:

$$p_{D_{j,h}, D_{j,k}} \prod_{l \leq D_{j,k}} a(k_l)$$

Here, the first term $p_{D_{j,h}, D_{j,k}}$ denotes the probability of traveling a distance $D_{j,k}$, given that the individual is currently at distance $D_{j,h}$ from their home location h . The second term captures the probability of choosing location k at that level distance, where $a(k_l)$ represents the attractiveness of a

container at level l that contains location k . Parameters H , a , and D are estimated for each individual via maximum likelihood estimation on the training data [16]. We generate 50 displacements per individual for evaluation on the test set.

- **Markov model.** Classical models for location prediction represent individual mobility as a Markov chain [71], where locations are treated as states and transitions between them are encoded in a Markov transition matrix. We implement a first-order Mobility Markov Chain (1-MMC) [69], in which the probability of visiting the next location depends only on the current one. During generation, the next location is sampled from the top three most likely locations based on the learned transition probabilities. This process is repeated until the generated sequence reaches the target length of 50 steps.
- **MHSA-based model.** Recent advances in next location prediction leverage deep sequential models that represent locations as latent embeddings and learn transition dynamics via attention-based architectures [72]. We train an MHSA network to autoregressively generate location sequences. At each step, the next location is sampled using a combination of top- k and nucleus sampling [73]. The top- k strategy restricts sampling to the k most probable candidates, while nucleus sampling limits it to the smallest set of locations whose cumulative probability exceeds a predefined threshold p . We set $k = 200$ and $p = 0.99$. The selected location is appended to the sequence and used as input for the next prediction step. This procedure is repeated for 50 steps.
- **MoveSim.** As a baseline for generative modeling of individual location choices, we implement MoveSim, a sequence-to-sequence model based on generative adversarial networks (GANs). The model consists of a generator that simulates location sequences using mobility priors, and a discriminator that distinguishes between real and generated sequences. These networks are trained jointly in an adversarial framework using a min-max objective. Unlike the original implementation, we exclude auxiliary features such as historical transitions, physical distances, and functional similarity, as they require pairwise location matrices that are computationally infeasible to construct given the large number of unique locations in our dataset.

We evaluate the performance of all models using established location-based metrics. In addition to those reported in the main text, we include the jump length distribution [7] and the uncorrelated entropy [11]. Results are shown in Supplementary Figure S1. To assess model fit, we compute the log-likelihood ratio, comparing the likelihood of the observed data under each model relative to MobilityGen. We addition-

ally calculate the Wasserstein distance to quantify discrepancies between empirical and model-generated distributions for each metric (Extended Data Table 1 and Supplementary Table S1). Overall, MobilityGen provides the closest approximation to the empirical data across all evaluated metrics, except for the jump length distribution, where it tends to overestimate the frequency of longer displacements (Supplementary Figure S1d). Moreover, the median evolution of the radius of gyration across individuals, $r_u(k)$, over displacement steps k , is well described by logarithmic growth (Supplementary Figure S1b). The fit $r_u(k) \propto \alpha \log(k)$, with parameters α derived from MobilityGen ($\alpha_{\text{MobilityGen}} = 2967 \pm 29$), aligns most closely with the real data ($\alpha_{\text{true}} = 2875 \pm 35$), while the baselines exhibit notably different values ($\alpha_{\text{epr}} = 6431 \pm 185$, $\alpha_{\text{container}} = 3784 \pm 68$, $\alpha_{\text{markov}} = 796 \pm 26$, $\alpha_{\text{mhsa}} = 1541 \pm 12$, $\alpha_{\text{movSim}} = 14976 \pm 462$). Collectively, the results show that MobilityGen more accurately captures key dimensions of location behavior, including visitation frequency, travel distance, and spatio-temporal spread, than traditional microscopic models.

Supplementary Note 1.2. Quantifying similarity and diversity in individual location sequences

To complement classical mobility metrics, we evaluate the simulated location sequences using metrics adapted from language modeling, which quantify both their similarity to and diversity from the real sequences. Similarity is measured using the Bilingual Evaluation Understudy (BLEU) score [74], an n-gram-based metric that compares each generated sequence to its corresponding ground truth, with higher values indicating greater similarity. We implement the smoothed sentence-level version of BLEU at n-gram levels 1 through 4 (BLEU-1 to BLEU-4), commonly used in sequence generation tasks. To evaluate intra-sequence diversity, we use the distinct unigram (dist-1) metric [62], which measures the proportion of unique locations within a sequence. Lower dist-1 values indicate higher repetition and less diversity. At the sequence level, we compute the diverse 4-gram (div-4) metric [75], which captures the proportion of distinct 4-grams in a sequence. Higher div-4 values indicate richer generation diversity. Evaluation results for all implemented microscopic mobility models are presented in Supplementary Table S2. Overall, MobilityGen produces location visit sequences that closely mirror real-world patterns, while avoiding input replication and preserving a realistic level of behavioral diversity.

While these metrics are informative, they should be interpreted with caution for the following reasons: (i) In contrast to language modeling, where multiple semantically valid reference sentences may exist, mobility datasets typically provide only one observed realization of an individual’s behavior, despite the existence of many plausible alternatives. (ii) Realistic mobility behavior involves a balance between exploration and habitual returns. As such, high diversity is not inherently desirable, and diversity metrics alone may not fully capture the plausibility of generated sequences.

Supplementary Note 2. Generating realistic activity event sequences

Supplementary Note 2.1. Comparison with spatio-temporal mobility simulators

To evaluate the effectiveness of MobilityGen in reproducing spatio-temporal activity-travel patterns, we benchmark its performance against two state-of-the-art mobility frameworks: the Diary-based Trajectory Simulator (DITRAS) [42] and TimeGeo [33]. Detailed descriptions of their methodologies and implementations are provided below.

- DITRAS decouples temporal pattern generation from spatial location assignment by modeling temporal dynamics with a mobility diary generator and assigning these diaries to physical locations using the density-EPR model [18]. The diary generator employs a time-aware Markov transition matrix to estimate transition probabilities between “typical” locations (e.g., home) and “non-typical” locations, along with the corresponding durations of stay. Non-typical locations are then assigned using the density-EPR mechanism, an extension of the classic EPR model that incorporates a relevance factor during exploration. We used the DITRAS implementation from scikit-mobility to align with our data format. Based on the training dataset, we estimated the population-level Markov transition matrix and calibrated individual-specific density-EPR parameters. Location relevance was determined by empirical visit frequencies. We adopted a temporal resolution of one hour and simulated 336 hourly steps per test sequence, corresponding to 14 days of spatio-temporal mobility.
- TimeGeo. Originally developed to reconstruct high-resolution spatio-temporal mobility trajectories from sparse digital traces, TimeGeo incorporates three individual-specific parameters to characterize temporal movement dynamics: the weekly number of home-based tours, the dwell rate, and the burst rate. These parameters govern time-dependent travel tendencies through a Markov decision process that distinguishes movement patterns based on an individual’s location state. Spatial decisions are modeled using a rank-based EPR mechanism, which selects exploration locations based on their proximity rank relative to the current location, rather than absolute geographic distance. We estimated temporal and spatial parameters for each individual using the training dataset. For each test sequence, the most frequently visited location was designated as the home location, and 336 consecutive hourly steps were simulated to generate a 14-day activity-travel trajectory.

We assess the performance of these models using mobility metrics that characterize activity-travel patterns. In addition to the metrics reported in the main text, we introduce two supplementary measures: the number of unique location visits per day and the distribution of activity start times. Evaluation results are

presented in Supplementary Figure S2. To quantify model performance, we compute the Wasserstein distance between the distributions of each metric derived from the generated activity events and those observed in the real data (Extended Data Table 3 and Supplementary Table S3). Metrics calculated from the source sequence are included as a strong reference baseline. However, it is important to account for variability in human activity behavior, as source sequences differ in both the duration and timing of activity events.

MobilityGen consistently outperforms all other models in capturing individual activity-travel patterns and interactions, demonstrating a substantial margin of improvement. Moreover, it simulates event sequences that are as accurate as, and in some cases even more accurate than, those derived from the source sequences.

Supplementary Note 2.2. Analysis of learned attribute embeddings

We examine the structure of the learned attribute embeddings to uncover how MobilityGen internalizes and organizes behavioral attributes. Each 128-dimensional embedding is projected onto a two-dimensional space using the densMAP method, as implemented in the Python library UMAP [76]. We use the default parameters ($\text{min_dist}=0.1$, $\text{dens_lambda}=2.0$) and confirm that alternative parameter combinations yield qualitatively consistent embedding structures. Two-dimensional visualizations are generated for both single attributes and composite activity events, computed according to Eq. 9.

Visualizations for travel mode, time, duration, and location are shown in Supplementary Figure S3. Travel modes with similar characteristics are positioned in close proximity within the embedding space; for example, walk and bike appear nearby, as do train, bus, and tram. In contrast, the “other” category appears isolated, reflecting its dissimilarity from all other modes. The time and duration embeddings in Supplementary Figure S3b and c form ordered, coherent trajectories, revealing that MobilityGen captures the continuous structure inherent in these attributes. For locations in Supplementary Figure S3d, the model organizes places according to their empirical visit frequencies in the training set, even though this frequency information is not explicitly observable from individual event sequences. This suggests that the model encodes the relative importance of locations based on usage patterns and implicitly captures the characteristic rank-frequency distribution observed in human mobility.

We next examine composite event embeddings (Supplementary Figure S4). Each point represents a mobility event defined by a combination of travel mode, time, duration, and location, with color denoting the visited location. A clear structural distinction emerges: some events form location-based clusters, while others are spatially mixed with no separation by destination. The embedding space thus loosely divides into an outer region of clustered behaviors and a central region of less location-dependent activity. This contrast suggests that the model distinguishes between different types of mobility behavior. We hypothesize

that these structural differences reflect underlying activity types; for example, routine visits such as home or work (spatially consistent) versus exploratory or irregular leisure activities (spatially diffuse). Because the embedding space encodes patterns learned directly from event sequences, it provides a valuable basis for analyzing how behavioral variations relate to spatial semantics and for advancing context-aware modeling of mobility behavior.

Supplementary Note 3. Role of behavioral and contextual factors

Supplementary Note 3.1. Effect of representing activity attributes and spatial context

We conduct ablation studies on MobilityGen to assess the contributions of activity attributes and contextual information. Activity attributes serve dual roles in the model: they are embedded jointly with location data to support the learning of mobility behavior (Eq. 9), and they provide additional supervisory signals through the loss function (Eq. 18). We begin with a model trained solely on location sequences and progressively incorporate time and travel mode attributes into the pipeline. All other training configurations are held constant to ensure a fair comparison. The results are summarized in Supplementary Table S4 and S5, where model performance is measured using the Wasserstein distance between generated and real sequences across a range of mobility metrics. Each model variant is simulated three times with different random seeds, and we report the mean and standard deviation of the resulting Wasserstein distances. While the base model, trained only on historical location data, already performs strongly relative to classical mobility baselines (see performance numbers in Extended Data Table 1 and Supplementary Table S1), the inclusion of either time or travel mode data leads to further improvements. The full model, which incorporates all behavioral attributes, achieves the best overall performance, with a slight decline observed only in the jump length metric. These findings support our claim that jointly modeling behavioral attributes results in a more realistic reproduction of individual mobility patterns.

Movement-related context, including location geometry and surrounding land-use functions, is integrated with activity attributes within the embedding space. We hypothesize that this integration enhances MobilityGen’s ability to characterize locations and is particularly useful for identifying novel locations for exploration. To evaluate this, we compare the full model with a variant that excludes contextual information. As described in the main text, generated locations are grouped into three sets based on their presence in the observed sequences: Set A includes locations common to both observed and generated data, while Sets B and C consist of locations unique to the observed and generated data, respectively. We then compute the Wasserstein distance to quantify discrepancies in the distribution of visits to functional areas. We expect

the model with contextual information to generate more similar visitation patterns for novel locations (i.e., comparisons between Sets B and C), and more distinct patterns between shared and novel locations (i.e., comparisons between Sets A and C), than the model without contextual information. This expectation is supported by the Wasserstein distance results in Supplementary Table S6, although the differences between models for Sets B and C are not statistically significant. This is likely due to the relatively low visit frequencies to these locations, which result in greater variability in visitation patterns.

Supplementary Note 3.2. Comparison with mobility flow prediction models

We benchmark MobilityGen against established flow models to evaluate how effectively it leverages contextual information when predicting mobility flows in unseen locations. We adopt the flow prediction task from Simini et al. [51], where the objective is to estimate the flow $y(l_i, l_j)$ between each origin-destination (OD) pair l_i and l_j per unit time, given the total outflow O_i from location l_i . That is, the task involves learning to distribute the total outflow from a given origin across all potential destinations based on location characteristics. Typical features include inter-location distance, population density, and contextual variables such as land use and POI types, which reflect the activity options available at each location. These correspond closely to the contextual inputs incorporated in MobilityGen.

To ensure consistency in temporal coverage and enable a fair comparison, we construct OD flow pairs from the test set of mobility event sequences. Locations are partitioned into two non-overlapping subsets: (i) \mathbb{S}_{seen} , comprising locations observed during the training period, and (ii) $\mathbb{S}_{\text{unseen}}$, containing locations that appear only during testing. Flow models are trained on OD pairs originating from \mathbb{S}_{seen} and evaluated on flows from $\mathbb{S}_{\text{unseen}}$, providing a direct assessment of generalization to novel locations. For MobilityGen, we aggregate simulated event sequences into OD flow pairs and evaluate performance exclusively on flows originating from $\mathbb{S}_{\text{unseen}}$. We next describe the flow models and feature sets used for comparison:

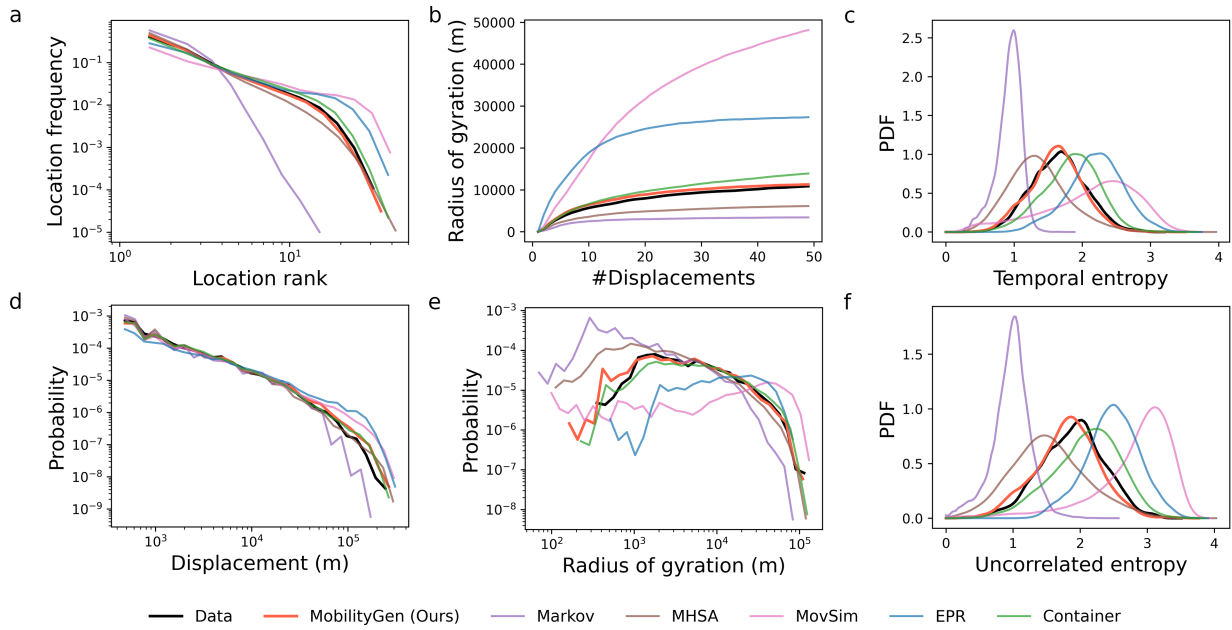
- Gravity [50]. We implement the singly constrained gravity model, which estimates flow $\hat{y}(l_i, l_j)$ from origin l_i to destination l_j based on population sizes m_i, m_j , and the distance d_{ij} :

$$\hat{y}(l_i, l_j) = O_i P_{ij} = O_i \frac{m_j^{\beta_1} f(d_{ij})}{\sum_k m_k^{\beta_1} f(d_{ik})}$$

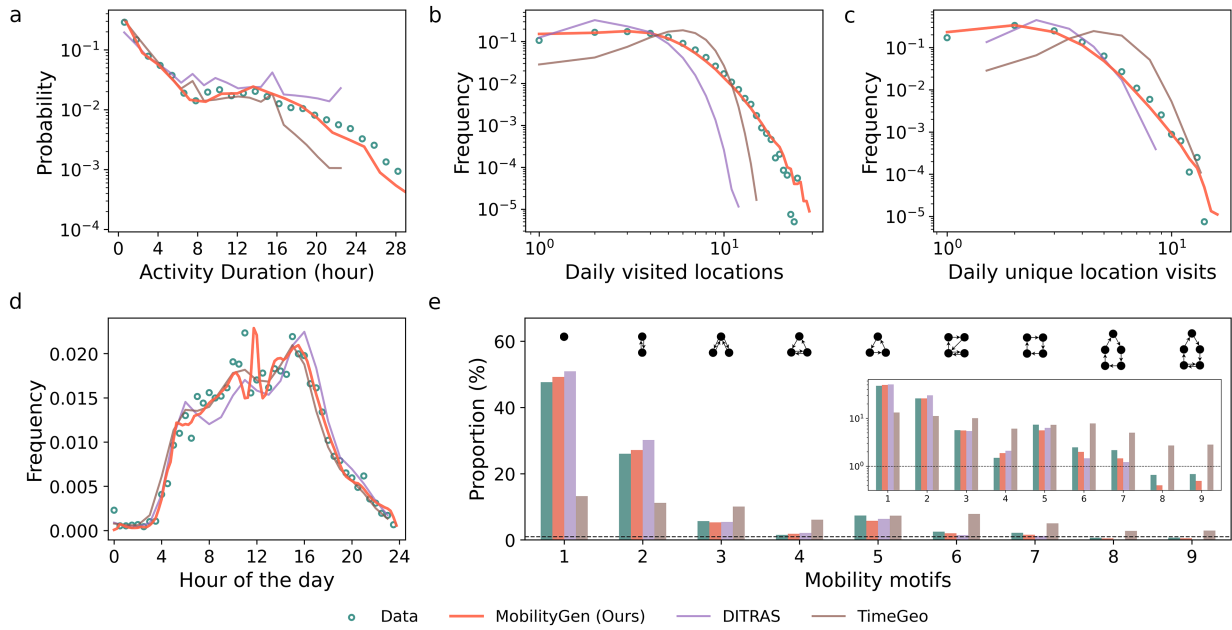
Here, P_{ij} denotes the normalized probability of travel from l_i to l_j , and $f(\cdot)$ is the deterrence function, specified as either exponential, $f(d) = \exp(\beta_2 d)$, or power-law, $f(d) = d^{\beta_2}$. The model parameters β_1 and β_2 are fitted to the training flows using maximum likelihood estimation. Preliminary experiments suggest slightly better performance using the power-law form.

- Deep Gravity [51]. This model generalizes the classical gravity framework by introducing hidden layers and nonlinearities, effectively converting it into a feedforward neural network. It incorporates additional geographic context for each location, including land use types, road network lengths, and counts of facilities related to transport, food, health, education, and retail. Each OD pair is described using 39 input features: 18 contextual attributes for both origin and destination, the distance between them, and their population sizes. We follow the original implementation, using the same feature set, architecture, and training procedure.
- Random Forest. We use the same 39 input features as Deep Gravity to train a random forest regressor for predicting OD flow intensities. Following the baseline configuration in Cabanas-Tirapu et al. [52], we employ 1000 estimators and the default hyperparameters from scikit-learn [77].

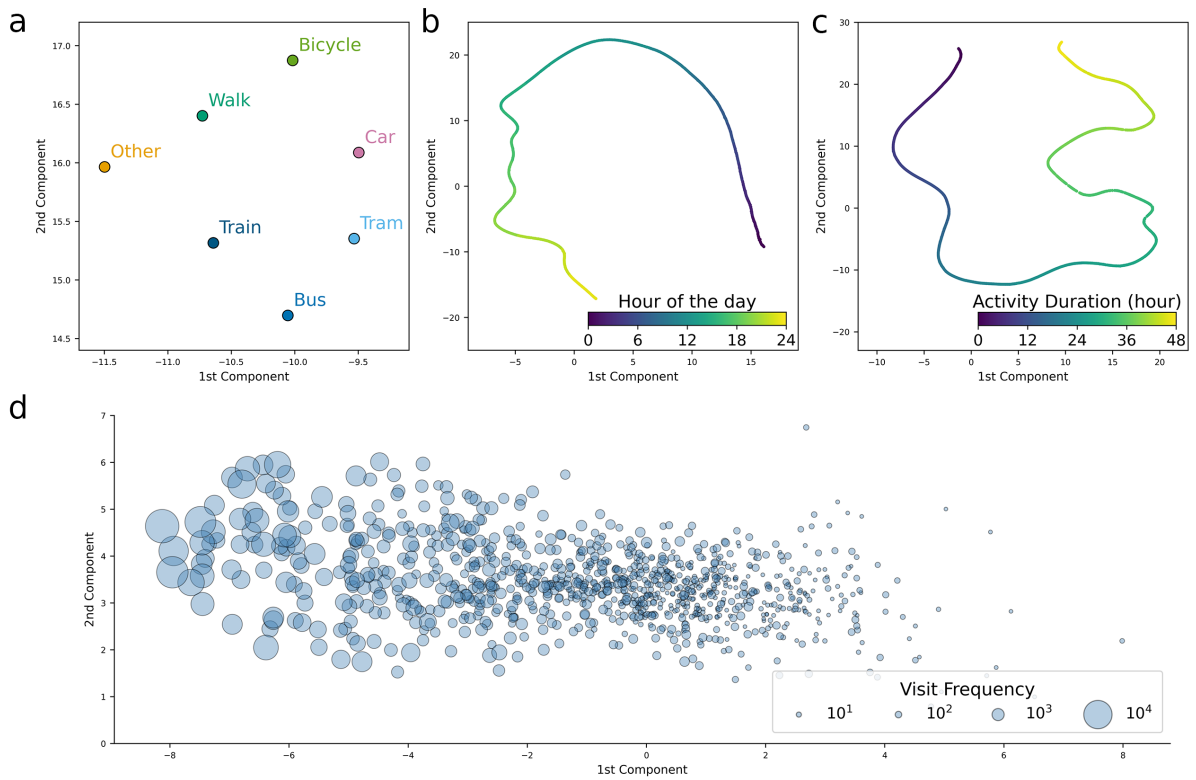
We evaluate model performance on flows originating from S_{unseen} using established mobility flow metrics: common part of commuters, Pearson correlation coefficient, and Jensen-Shannon divergence. Summary results are presented in Extended Data Table 4. To further assess spatial distributions, we compute the entropy of disaggregated destination probabilities. These are compared with empirical distributions and those generated by MobilityGen. Across all metrics, MobilityGen consistently achieves the highest performance and most closely reproduces the observed spatial distribution of location visits, outperforming all baseline models. We attribute these gains to the integration of detailed spatial features (e.g., urban function distributions via LDA) alongside the joint modeling of contextual and behavioral factors.



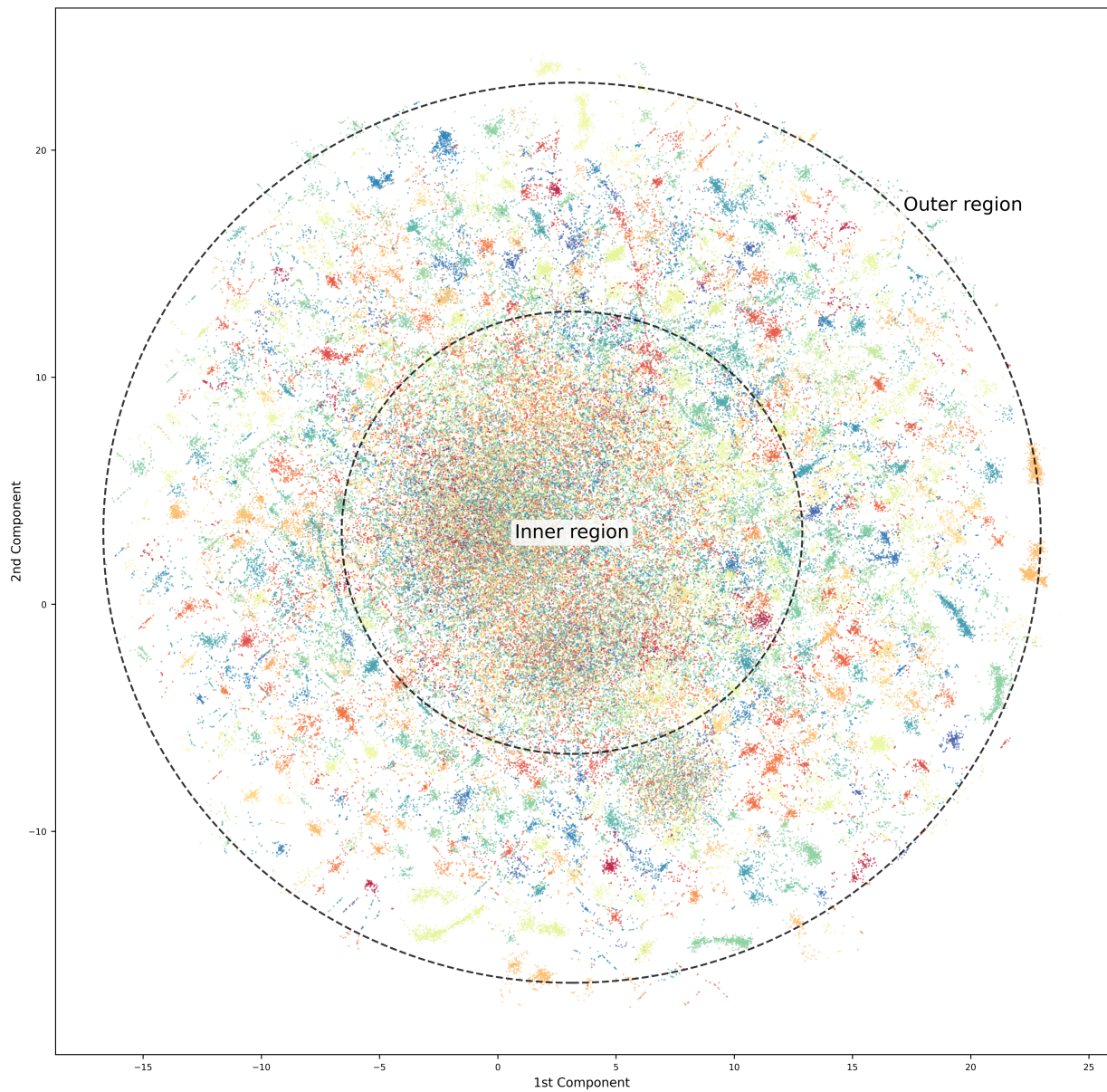
Supplementary Figure S1: Evaluating microscopic mobility models with location metrics. **a.** Rank-frequency distribution of visited locations. **b.** Median radius of gyration as a function of the number of displacements. **c.** Distribution of temporal mobility entropy across individuals. **d.** Distribution of displacements for the entire population. **e.** Distribution of radius of gyration across individuals. **f.** Distribution of uncorrelated mobility entropy across individuals. These metrics are compared between real data (black) and traces generated by MobilityGen (red), Markov (purple), MHSA (brown), MovSim (pink), EPR (blue), and Container (green).



Supplementary Figure S2: Generated events replicate individual activity-travel patterns and interdependencies. **a.** Distribution of activity durations. **b.** Distribution of daily visited locations. **c.** Distribution of daily unique visited locations. **d.** Distribution of activity start times throughout the day. **e.** Distribution of mobility motifs, with motif diagrams shown above. The dashed line marks the 1% threshold as a visual guide, and the inset presents the same distribution on a log scale. Metrics are compared between real data (green) and activity events generated by MobilityGen (red), DITRAS (purple), and TimeGeo (brown).



Supplementary Figure S3: Visualization of learned activity embeddings. 2D projections of the 128D attribute embeddings, obtained using the densMAP algorithm ($\text{min_dist}=0.1$, $\text{dens_lambda}=2.0$). **a.** Travel mode embeddings reveal interpretable structure: similar modes (walk and bike; bus, tram, and train) are positioned closely, while “other” appears isolated. **b.** Time embeddings form a continuous trajectory that progresses over the 24-hour day, with neighboring hours mapped to adjacent regions. **c.** Duration embeddings follow a similarly ordered curve, reflecting the gradual increase from 0 to 48 hours. **d.** Location embeddings are structured by visit frequency, with marker size denoting log-scaled frequency. Higher-frequency locations cluster toward one end of the space.



Supplementary Figure S4: Visualization of learned event embeddings. Each point represents a mobility event defined by a unique combination of travel mode, time, duration, and location, with colors indicating the visited location. The embedding space shows a clear structural distinction between two loosely defined regions: an outer region where events form location-based clusters, and an inner region where events are mixed without clear spatial separation. The circular boundaries serve as visual guides to illustrate the transition from disordered to clustered patterns. This contrast suggests that the model distinguishes between different types of mobility behavior.

Supplementary Table S1: Supplementary performance using additional location metrics. The log-likelihood ratio measures the likelihood that the real data was generated by each model relative to MobilityGen, with positive values favoring MobilityGen (all $P < 10^{-3}$, except for $P(f_{\Delta r})$ in MHSA, where $P = 0.66$). The Wasserstein distance assesses the dissimilarity between generated and real location metric distributions, with higher values indicating greater divergence. Results are presented for jump length ($f_{\Delta r}$), radius of gyration (f_{r_u}), and uncorrelated entropy (S_{unc}); best-performing values are shown in bold.

	Log-likelihood			Wasserstein distance		
	$P(f_{\Delta r})$	$P(f_{r_u})$	$P(S_{\text{unc}})$	$f_{\Delta r}$	f_{r_u}	S_{unc}
EPR	166326	31364	74711	15882	12825	0.60
Container	-6568	946	2741	1146	3578	0.20
Markov	2697	16530	329477	2223	10102	0.91
MHSA	-115	4352	8355	1491	5137	0.35
MovSim	35384	79922	48838	8128	34096	0.92
MobilityGen (Ours)	-	-	-	2318	575	0.08

Supplementary Table S2: Sequence similarity and diversity with language modeling metrics. The BLEU score quantifies similarity between generated and real location sequences, with higher values indicating better alignment. Distinct unigrams (dist-1) and diverse 4-grams (div-4) measure sequence diversity at the intra-sequence and inter-sequence levels, respectively, where higher values indicate greater variability.

	BLEU	dist-1	div-4
Markov	0.28	0.08	0.02
MHSA	0.24	0.21	0.29
MovSim	0.002	0.51	0.60
EPR	0.09	0.42	0.77
Container	0.19	0.31	0.57
MobilityGen (Ours)	0.26	0.23	0.34

Supplementary Table S3: Additional metrics for behavioral alignment. The Wasserstein distance quantifies dissimilarities between metric distributions derived from simulated and real activity events. Results are presented for unique daily visited locations ($f_{|k|}^{\text{day}}$) and activity start times (f_t); best-performing values are shown in bold.

	$f_{ k }^{\text{day}}$	f_t
DITRAS	0.37	1.49
TimeGeo	1.78	1.48
MobilityGen (Ours)	0.22	0.52

Supplementary Table S4: Ablation study on activity attributes (location metrics). The full model is compared to reduced variants: one using location only (base), and others including time (base + time use) or travel mode (base + travel mode). Wasserstein distances are reported for number of visits per location (f_k), jump length ($f_{\Delta r}$), radius of gyration (f_{r_u}), temporal entropy (S_{temp}), and uncorrelated entropy (S_{unc}); best-performing values are shown in bold.

	f_k	$f_{\Delta r}$	f_{r_u}	S_{temp}	S_{unc}
Base	0.649 \pm 0.003	3871 \pm 16	901 \pm 21	0.110 \pm 0.0004	0.216 \pm 0.001
Base + time use	0.543 \pm 0.002	2280 \pm 21	625 \pm 19	0.101 \pm 0.0005	0.144 \pm 0.001
Base + travel mode	0.519 \pm 0.002	3493 \pm 15	804 \pm 13	0.088 \pm 0.0003	0.136 \pm 0.001
Full model	0.262 \pm 0.004	2318 \pm 14	574 \pm 17	0.036 \pm 0.001	0.080 \pm 0.001

Supplementary Table S5: Ablation study on activity attributes (activity-travel metrics). The full model is compared to reduced variants: one incorporating only time (base + time use) and another incorporating only travel mode (base + travel mode). Wasserstein distances are reported for activity duration (f_d), activity start time (f_t), daily visited locations (f_k^{day}), unique daily visited locations ($f_{|k|}^{\text{day}}$), mobility motifs (f_{motifs}), and travel mode (f_m); best-performing values are shown in bold.

	f_d	f_t	f_k^{day}	$f_{ k }^{\text{day}}$	f_{motifs}	f_m
Base + time use	0.904 \pm 0.01	0.73 \pm 0.01	0.447 \pm 0.002	0.273 \pm 0.001	0.233 \pm 0.01	-
Base + travel mode	-	-	-	-	-	0.113 \pm 0.001
Full model	0.473 \pm 0.001	0.52 \pm 0.01	0.292 \pm 0.01	0.224 \pm 0.002	0.142 \pm 0.004	0.048 \pm 0.002

Supplementary Table S6: Ablation study on contextual information. The full model is compared to a variant without contextual inputs (MobilityGen w/o ctx). Locations are grouped based on their presence in real and generated sequences. Wasserstein distances quantify differences in the distribution of visits to functional areas, including Set A (real) vs. Set A (generated) (d_A), Set C vs. Set B (d_B^C), Set C vs. Set A (real) ($d_{A_{observe}}^C$), and Set C vs. Set A (generated) ($d_{A_{generate}}^C$). Arrows indicate whether smaller or larger values are preferred.

	$d_A \downarrow$	$d_B^C \downarrow$	$d_{A_{observe}}^C \uparrow$	$d_{A_{generate}}^C \uparrow$
MobilityGen w/o ctx	0.025 \pm 0.001	0.153 \pm 0.067	0.548 \pm 0.001	0.545 \pm 0.001
MobilityGen	0.009 \pm 0.001	0.105 \pm 0.006	0.560 \pm 0.005	0.558 \pm 0.003